Journal of Asian Earth Sciences

GEOLOGY, MINERALIZATION AND MAGMA EVOLUTION OF THE ZUUN MOD MO-CU DEPOSIT IN SOUTHWEST MONGOLIA

--Manuscript Draft--

Manuscript Number:	JAESS-D-23-00283R1
Article Type:	Research Paper
Keywords:	Porphyry Mo-Cu deposit, Zuun Mod, Zircon U-Pb geochronology, Re-Os geochronology, southwest Mongolia
Corresponding Author:	Enkhjargal Boldbaatar, Ph.D. Mongolian University of Science and Technology MONGOLIA
First Author:	Altankhuyag Gankhuyag, M.D
Order of Authors:	Altankhuyag Gankhuyag, M.D
	Enkhjargal Boldbaatar, Ph.D.
	Bolorchimeg N. Tunnell, Ph.D.
	Jargalan Sereenen, Ph.D.
	Marek Locmelis, Ph.D.
	Xiaofeng Li, Ph.D.
	Akira Imai, Ph.D.
Abstract:	Zuun Mod is a porphyry-type Mo-Cu deposit located in the Edren terrane in southwest Mongolia. The deposit has estimated resources of 218 Mt with an average Mo grade of 0.057% and Cu grade of 0.069%, and significant amounts of Re. The deposit is characterized by multiple pulses of magmatism and exsolution of magmatic ore fluids and associated alteration and mineralization. The timing of these events and the tectonic environment were unconstrained, and its genesis controversial. Based on drill core and field examinations, four lithological units of the Bayanbulag intrusive complex are identified in the deposit area including quartz syenite, quartz monzonite, granodiorite, and granite. The majority of Mo mineralization at Zuun Mod occurs in sheeted and stockwork quartz veins that crosscut units of the Bayanbulag complex as well as disseminations within altered granitoids wherein the mineralized quartz veins occur with potassic and phyllic alteration selvages. Zircon U-Pb age dating for quartz monzonite and granodiorite defined the timing of magmatic events at 305.3 ± 3.6 Ma and 301.8 ± 2.7 Ma, respectively. Molybdenite Re-Os geochronology on grains from a quartz vein with potassic alteration selvage was determined at 297±4.8 Ma, indicating the age of Mo mineralization. Lithogeochemical data of intrusive units suggest the granitoid rocks show calc-alkaline to high-K calc-alkaline, I-type, and metaluminous to slightly peraluminous affinities that formed in a post-collisional setting and were likely sourced from subduction-modified lithosphere. Lithogeochemical signatures and the tectonic environment classify Zuun Mod into neither Climax nor Endako-types, but as a Mo-rich porphyry Cu deposit.
Suggested Reviewers:	Doug Kirwin, Ph.D. Adjunct Professor, James Cook University Queensland Research Centre for Peripheral Vascular Disease djkdoug@gmail.com He is an expert in porphyry deposit, he worked in porphyry deposits in Mongolia.
	Antonio Arribas, Ph.D. Professor, The University of Texas at El Paso aarribas@utep.edu He is an expert in economic geology
Opposed Reviewers:	

Geology, Mineralization and Magma Evolution of the Zuun Mod Mo-Cu Deposit in Southwest Mongolia

Gankhuyag Altankhuyag [a], Enkhjargal Boldbaatar [a*], Bolorchimeg N. Tunnell [a], Jargalan Sereenen [a], Marek Locmelis [b], Xiaofeng Li [c, d], Akira Imai [e]

[a] Department of Geology and Hydrogeology, School of Geology and Mining Engineering, Mongolian University of Science and Technology, Ulaanbaatar, Mongolia
[b] Department of Geosciences and Geological and Petroleum Engineering, Missouri University of Science and Technology, Rolla, Missouri, USA
[c] Key Laboratory of Mineral Resources, Institute of Geology and Geophysics, Chinese Academy of Sciences, Beijing, China
[d] College of Earth and Planetary Sciences, University of Chinese Academy of Sciences, Beijing, China Institute
[e] Department of Earth Resources Engineering, Faculty of Engineering, Kyushu University, Fukuoka, Japan

Abstract

Zuun Mod is a porphyry-type Mo-Cu deposit located in the Edren terrane in Southwest Mongolia. The deposit has estimated resources of 218 Mt with an average Mo grade of 0.057% and Cu grade of 0.069%, and significant amounts of Re. The deposit is characterized by multiple pulses of magmatism and exsolution of magmatic ore fluids and associated alteration and mineralization. The timing of these events and the tectonic environment were unconstrained, and its genesis controversial. Based on drill core and field examinations, four lithological units of the Bayanbulag intrusive complex are identified in the deposit area including quartz syenite, quartz monzonite, granodiorite, and granite. The majority of Mo mineralization at Zuun Mod occurs in sheeted and stockwork quartz veins that crosscut units of the Bayanbulag complex as well as disseminations within altered granitoids wherein the mineralized quartz veins occur with potassic and phyllic alteration selvages. Zircon U-Pb age dating for quartz monzonite and granodiorite defined the timing of magmatic events at 305.3 ± 3.6 Ma and 301.8 ± 2.7 Ma, respectively. Molybdenite Re-Os geochronology on grains from a quartz vein with potassic alteration selvage was determined at 297±4.8 Ma, indicating the age of Mo mineralization. Lithogeochemical data of intrusive units suggest the granitoid rocks show calc-alkaline to high-K calc-alkaline, I-type, and metaluminous to slightly peraluminous affinities that formed in a post-collisional setting and were likely sourced from subduction-modified lithosphere. Lithogeochemical signatures and

the tectonic environment classify Zuun Mod into neither Climax nor Endako-types, but as a Mo-rich porphyry Cu deposit.

Keywords: Porphyry Mo-Cu deposit, Zuun Mod, Zircon U-Pb geochronology, Re-Os geochronology, Southwest Mongolia

***Corresponding author:** Enkhjargal Boldbaatar; enkhjargal2404@must.edu.mn; Department of Geology and Hydrogeology, School of Geology and Mining Engineering, Mongolian University of Science and Technology, Ulaanbaatar, Mongolia

1. Introduction

Porphyry-type deposits are the primary source of Cu and Mo, accounting for up to 75% of the global Cu and nearly 99% of global Mo production (Richards, 2003; Seedorff et al., 2005; Sillitoe, 2010). Additionally, porphyry deposits are major repositories of Au, Ag, and Sn, as well as some other byproducts such as Re, W, In, Pt, Pd, Se, Te, Bi, Pb, and Zn (John and Taylor, 2016; Sillitoe, 2010; Sinclair, 2007). Approximately half of the molybdenum production comes from porphyry Mo deposits in which Mo is the primary recoverable metal with Mo:Cu ratios greater than 1 and ore grades exceeding 0.05 wt % Mo (Sinclair, 2007). The remaining 50% of Mo is recovered from porphyry Cu-Mo deposits as a byproduct.

The formation of porphyry deposits is associated with subduction- and collision-related magmatism in orogenic belts (Hou and Cook, 2009; Hou et al., 2011; Sillitoe, 2010; Sinclair, 2007; Sun et al., 2015). The Central Asian Orogenic Belt (CAOB), which extends from the Ural Mountains in Russia and Kazakhstan to Northeastern China, is the world's largest and longest-lived (ca. 1000-250 Ma) orogenic belt, and hosts more than 20 major Cu-Mo, Mo-Cu, and Cu-Au porphyry deposits (Khain et al., 2002; Seltmann et al., 2014; Windley et al., 2007; Xiao et al., 2003). Mongolia, located in the central part of the CAOB, hosts several large porphyry deposits (Fig. 1A), including the world class Oyu Tolgoi Cu-Au-(Mo) deposit (Khashgerel et al., 2006; Wainwright et al., 2011a; 2011b), as well as the Kharmagtai Cu-Au (Kirwin et al., 2005; Vigar et al., 2015) and Tsagaan Suvarga Cu-Mo deposits (Tungalag et al., 2019; Watanabe and Stein, 2000). These porphyry deposits generally occur in island arc terranes, including the Edren terrane located in southwestern

Mongolia. The Edren terrane hosts several less explored porphyry deposits such as the Zuun Mod Mo-Cu porphyry, Khul Morit Cu-Au porphyry, Shalyn Khudag Cu-Mo porphyry, Senjit Khyar Cu porphyry, Khuis Tolgoi Cu porphyry, and Chandmani Uul Cu porphyry deposits, as well as several genetically associated epithermal deposits, including the Bayan Khundii Au and Altan Nar Au-polymetallic deposits (Fig. 1B). Among these deposits, the Zuun Mod deposit is the largest, and was first noted as a prospect during a geologic mapping project at a scale of 1:200.000 between 1996 and 1999 (Bukhbat et al., 1999). Subsequent exploration projects, including one conducted by a joint venture between WMC Resource Project Ltd and Gallant Minerals Mongolia Ltd between 2002 and 2003 and another by Erdene Resource Development Corporation between 2005 and 2008 identified the Zuun Mod deposit as a porphyry Mo-Cu type based on the geological setting, host rock alterations, and type of mineralization (Corey et al., 2006; Gillis, 2007; Osterman, 2003). The Mo-Cu mineralization at Zuun Mod is hosted in the late Carboniferous Bayanbulag intrusive complex and associated stockwork and sheeted quartz veins and veinlets developed within the intrusive complex (Altankhuyag, 2008; Bat-Erdene et al., 2011; Gillis, 2007; Gonchigjav et al., 2010). The deposit's estimated resources are 218 Mt of ore with an average Mo grade of 0.057% and an average Cu grade of 0.069% (Clark and Baudry, 2011; Gonchigjav et al., 2010). Additionally, the deposit locally contains significant amounts of Re with grades varying between 0.15 ppm and 0.29 ppm Re within molybdenite mineralized zones and contents as high as 125 to 150 ppm Re in individual molybdenite grains (Clark and Baudry, 2011; Gillis, 2007).

Although resource estimates and broad stratigraphic relationships have been reported previously, the genesis of the Zuun Mod deposit remains poorly understood and discussions on its origin are largely restricted to technical reports. For example, an early technical report on exploration results by Gillis (2007) speculates that the Zuun Mod deposit might be a British Columbia (BC) type deposit based on intermediate composition host rocks, high Cu concentrations, and overall fluorine-poor nature, although locally abundant fluorite and topaz are observed in some of the molybdenite-bearing veins. A later technical report by Clark and Baudry (2011) classified the deposit as a transitional style of porphyry Mo deposit between Climax and Endako types based on ore grades, the presence of fluorite, and petrographic examination. In contrast, Taylor et al. (2012) identified the Zuun Mod deposit as a possibly arc-related Endako-type based on the data and/or studies available to these authors. The intrusive body that is spatially and temporally associated with the Zuun Mod Mo-Cu mineralization has been assumed to be Carboniferous based on geological relationships

(Bukhbat et al., 1999), or late Carboniferous based on geological relationships wherein the Bayanbulag complex intrudes the early Carboniferous Khuviinkhar Formation whose age was defined as early Carboniferous by fossilized flora (Togtokh and Gunbileg, 2013; Zabotkin et al., 1988). That said, the precise age of the host rocks has not been determined.

Here we report the first results of a lithogeochemical and zircon U-Pb geochronological study of the ore-hosting intrusive rocks of the Bayanbulag intrusive complex. We also report the first mineralization age for the Zuun Mod deposit using molybdenite Re-Os analysis. The data are integrated with geological and mineralogical observations (including alteration features) to better understand the origin of the Zuun Mod deposit.

2. Geological background

The Zuun Mod porphyry Mo-Cu deposit is located in the Edren terrane in Southwest Mongolia (Fig. 1), a dissected section of the Kazakh-Mongol magmatic arc which is part of the Transbaikal-Mongolian tectonic collage (Yakubchuk, 2002, 2005; Yakubchuk et al., 2002). Together with the Altaid tectonic collage to the west, these orogenic collages form the CAOB that records 750 Ma of continental growth through continuous subduction-accretion within the long-lived Paleo-Asian Ocean from the Neoproterozoic through Paleozoic eras (Dobretsov et al., 2004; Kuzmichev et al., 2005; 2007; Yarmolyuk et al., 2006). The CAOB is surrounded by the Siberian craton to the north and the North China and Tarim cratons to the south (Dobretsov et al., 1995; Jahn et al., 2000), and extends from the Ural Mountains in Kazakhstan and Russia to the west through Kazakhstan, northern China, Mongolia, southern Siberia, and northeastern China to the Pacific coast on the east (Kröner et al., 2007; Sengör et al., 1993; Yakubchuk, 2002). Generally, two different models have been proposed to explain the continental growth in the CAOB. Sengör et al. (1993) and Sengör and Natal'in (1996) proposed a model wherein the orogen formed by successive subduction-accretion and oroclinal bending of a single giant (i.e., ~7000 km long) long-lived volcanic arc system. Other models suggest that small ocean basins were closed along several subduction zones through the accretion of island arcs, oceanic islands, seamounts, microcontinents, and obduction of ophiolites (Badarch et al., 2002; Khain et al., 2003; Kuzmichev et al., 2005; Mossakovsky et al., 1993). Regardless of these models, the assembly of the CAOB in the Neoproterozoic to Mesozoic produced major growth of the continental crust (Sengör et al., 1993).

Mongolia, located at the center of the CAOB, is subdivided into northern and southern domains separated by the so-called Main Mongolian Lineament (Fig. 1A; Badarch et al., 2002; Yakubchuk, 2005) which is considered to be a section of the CAOB-wide Irtysh fault (Yakubchuk et al., 2012). The northern domain is usually classified as a 'Caledonian' orogen which is composed of cratonal fragments of Precambrian rocks dislocated by faults, late Neoproterozoic to Ordovician Tuva-Mongol magmatic arc intrusions, and associated sequences of series of back-arc and fore-arc, accretionary wedge, ophiolite, and Proterozoic to lower Paleozoic intrusions (Badarch et al., 2002). The southern domain is a Hercynian (or Variscan) orogen dominated by Silurian to latest Carboniferous arc-related magmatic and volcano sedimentary rocks that were intruded by rift-related bimodal and alkali granitic magmatism during the latest Carboniferous – earliest Permian (Badarch et al., 2002; Lamb and Badarch, 1997). During the evolution of the Caledonian and Hercynian orogenic belts, some of the subduction-related magmatic events resulted in the formation of porphyry Cu, Au, and Mo deposits such as those shown in Figure 1 (Badarch et al., 2002).

The Edren terrane is considered to be an ensialic island arc developed on the distal southern margin of the Siberian paleocontinent within the southern Mongolian Hercynian paleo-ocean that existed between the late Silurian and Carboniferous (Dergunov, 2001; Ruzhentsev et al., 1990). The Edren terrane is divided into a northern (Khuviinkhar) and southern (Edren) subsequence (Badarch et al., 2002; Lamb and Badarch, 1997). The northern Khuviinkhar sequence consists of Devonian terrigenous sedimentary and volcanic rocks as well as Carboniferous terrigenous sedimentary rocks (Badarch et al., 2002; Tumurkhuu et al., 2010). The rocks of the Khuviinkhar sequence have undergone intense brittle deformation, folding, and shearing, which resulted in greenschist metamorphism (Badarch et al., 2002). The folds on the northern margin of the Edren terrane suggest dextral strike-slip displacement along the Bulgan fault which separates the terrane from the northern block (Fig. 1B; Badarch et al., 2002). The southern Edren subsequence is dominated by Devonian and Lower Carboniferous basalts, andesites, volcanic breccias, tuffs, volcaniclastic rocks, cherts, minor limestones, and clastic sediments that locally contain early Devonian gabbroic sill-like bodies (Yarmolyuk and Tikhonov, 1982). The major and trace element chemistry of Devonian basalts show medium- to high-K calc-alkaline affinities similar to gabbroic bodies, thus suggesting an arc environment (Lamb and Badarch, 1997; Togtokh et al., 2020; Tumurkhuu et al., 2013). The Edren terrane was intruded by fewer Devonian and more widespread Carboniferous diorites, granodiorites, as well as tonalitic plutons and lesser early Permian granitic rocks, all of which are overlain by late Permian felsic and volcanic rocks (Badarch et al., 2002; Togtokh et al., 2020). Carboniferous intrusive rocks are spatially and temporally associated with a number of porphyry Cu-Au and Mo-Cu deposits and occurrences that have been discovered during exploration campaigns in the region over the past several decades (Fig. 1B; Delgertsogt et al., 2014).

3. Geology of the Zuun Mod porphyry Mo-Cu deposit

The Zuun Mod porphyry Mo-Cu deposit is located in the NE-SW trending contact fault between the early Carboniferous Khuviinkhar Formation and the Bayanbulag intrusive complex (Fig. 2A; Corey et al., 2006; Gillis, 2007; Gonchigjav et al., 2010). The Khuviinkhar Formation consists of a succession of basalts, basaltic andesites, andesites, andesitic dacites, and their tuffs, the age of which was determined as Tournaisian and Visean (359-330 Ma) based on fossilized flora (Fig. 2; Bukhbat et al., 1999; Gonchigjav et al., 2010; Zabotkin et al., 1988). In the area of the Zuun Mod deposit, the Bayanbulag intrusive complex consists of quartz syenites, quartz monzonites, granodiorites, and granites. Drill core observations indicate that the quartz syenite and quartz monzonite units were intruded by the granodiorites and granites (Fig. 2B; Altankhuyag, 2008; Bat-Erdene et al., 2011; Corey et al., 2006; Gillis, 2007; Gonchigjav et al., 2010) .

3.1. Bayanbulag intrusive complex

Based on field relationships and drill core observation, the quartz syenite, located in the uppermost part of the Bayanbulag intrusive complex and outcropping south of the fault in the area of the Racetrack South orebody (Fig. 2), is the earliest intrusion unit in the deposit area. Drill core observations suggest the quartz syenite is less mineralized compared to quartz monzonite and granodiorite. Nevertheless, quartz syenite typically contains lower concentrations of Mo due to the intrusion of quartz monzonite, granodiorite, and granodiorite porphyry. Drill core intercepts of mineralized zones at depths of 150-550 m indicate that the mineralization is restricted to stockwork and sheeted quartz veins and veinlets hosted in potassic altered quartz monzonite, granodiorite, and lesser quartz syenite.

The quartz monzonite is pink to pinkish-red and medium to coarse-grained with a seriate texture. It contains abundant quartz, potassium feldspar, and plagioclase with minor biotite and hornblende, as well as ore minerals such as magnetite and sulfides (Figs. 3A, B, C). It is noteworthy that at the surface, plagioclase is replaced by clay minerals. At depths greater than 150 m, plagioclase is replaced by potassium feldspar, forming potassic alteration halos together with magnetite, biotite, and, locally, chalcopyrite and molybdenite. Quartz monzonite is also crosscut by quartz veins and veinlets with up to 10-15 modal percent molybdenite (Fig. 3B). In areas of extensive veining, potassic vein selvages coalesce, resulting in the formation of pervasive potassically altered rocks (Fig. 3C). The quartz monzonite is intruded by a granodiorite unit that itself was intruded by a biotite granite. The granodiorite is gray and fine- to medium-grained with a seriate texture and contains plagioclase, quartz, biotite, and lesser potassium feldspar and hornblende (Figs. 3D, E, F). The granodiorite is intensely crosscut by sheeted and stockwork quartz veins that contain moderate to intense (10-15 modal abundances) Mo mineralization. The biotite granite is the latest phase of the Bayanbulag complex. It is pinkish gray, medium- to coarse-grained with equigranular texture, and is composed of quartz, potassium feldspar, plagioclase, biotite, hornblende, and minor magnetite and sulfides (Figs. 3G, H). Hydrothermal alteration and quartz veins are common in both the granodiorite and biotite granite units.

3.2. Structure of the deposit and Mo-Cu mineralization

Molybdenum and Cu mineralization occurs in stockwork and sheeted quartz zones that crosscut the compositionally different granitoid rocks wherein the ore grades increase with increasing quartz veins density (Altankhuyag, 2008; Bat-Erdene et al., 2011; Gillis, 2007; Gonchigjav et al., 2010). The area of the Zuun Mod deposit is characterized by the presence of an approximately circular structure with a diameter of 4-5 km (indicated in Fig. 2A) that was identified through magnetic and geochemical anomalies, as well as NE-SW, NW-SE, and E-W-trending faults (Corey et al., 2006; Gillis, 2007; Gonchigjav et al., 2010). The NE and NW fault are interpreted to have formed as a conjugate fault set reflecting N-S compression related to subduction (Clark and Baudry, 2011; Gillis, 2007). The E-W faults formed post-mineralization and controlled the emplacement of dykes that formed an intense superimposed fracture-cleavage in some places (Clark and Baudry, 2011; Gillis, 2007). The preferred NE and NW orientation of mineralized intrusive units, quartz zones, and porphyry-related alteration zones indicate that mineralized fluids were focused primarily within these structural corridors (Clark and Baudry, 2011; Gillis, 2007). Exploration campaigns conducted by the WMC Ltd/Gallant Ltd joint venture and Erdene Resources Ltd from 2002 to 2009 identified three different orebodies, i.e., the Racetrack South, Racetrack North, and Stockwork ore bodies (Fig. 2A). The ore bodies occur along the NE-SW trending structurally controlled zone, striking at an angle of 45° within the so-called South Corridor, which extends over 3.6 km distance with a width of 800 m (Fig. 2; Bat-Erdene et al., 2011; Gillis, 2007; Gonchigjav et al., 2010).

Racetrack South: The Racetrack South orebody is hosted within quartz monzonite and granodiorite and forms an up to 1.1 km long and 400 m wide body (Figs. 2; 3A, B, C; Bat-Erdene et al., 2011; Gillis, 2007; Gonchigjav et al., 2010). Molybdenum mineralization occurs as disseminated molybdenite within the alteration halos of the quartz monzonite and granodiorite replacing primary and secondary magnetite and biotite (Fig. 3A), as well as stockwork and sheeted quartz veins and veinlets filling open spaces and fractures (Figs. 3B, C; Gillis, 2007; Gonchigjav et al., 2010). Pyrite and chalcopyrite locally replace magnetite and biotite within the host granitoids (Altankhuyag, 2008; Gillis, 2007; Gonchigjav et al., 2010). Molybdenum grades from 200 to 900 ppm Mo with Cu contents between 500 to 1000 ppm Cu.

Racetrack North: Racetrack North is an up to 1.1 km long and 300-500 m wide ore body with mineralized stockwork (dominant) and sheeted quartz veins hosted in granodiorites (Figs. 2; 3D, E; Altankhuyag, 2008; Bat-Erdene et al., 2011; Gillis, 2007; Gonchigjav et al., 2010). The thickness of sheeted and stockwork quartz veins and veinlets ranges from 0.1 to 3.0 cm and fills open spaces and fractures. The ore veins/veinlets are characterized by quartz±molybdenite±chalcopyrite±pyrite in association with potassically altered selvages composed of potassium feldspar, secondary biotite, and magnetite (Fig. 3E; Clark and Baudry, 2011; Gillis, 2007). Disseminated molybdenite, chalcopyrite, and pyrite are also found within the halos of the potassically altered host granodiorite where they replace biotite and/or are intergrown with secondary biotite and magnetite (Fig. 3E). Rare fractures filled with massive molybdenite and thicknesses up to 0.5 cm have also been observed cf. (Bat-Erdene et al., 2011; Gonchigjav et al., 2010). The molybdenum ore grades from 100 to 2000 ppm Mo with copper contents from 200 to 500 ppm Cu. Potassic and sericitic alterations are observed rimming the quartz veins and veinlets, while granodiorite entirely shows phyllic alteration composed of quartz-sericite-pyrite.

Stockwork: The Stockwork orebody occurs in the southern portion of the circular structure and is an up to 500 m-long and 300 m-wide ore body hosted in quartz monzonites and granodiorites (Figs. 2; 3F; Gillis, 2007). Molybdenum and copper mineralization occurs as stockwork veins and veinlets, as well as disseminated within the intensely altered granitoids by replacing mafic minerals (Fig. 3F). Quartz+pyrite±molybdenite±chalcopyrite stockwork veining is widespread, particularly in drill hole KKMD-03 which intersected a 238 m zone with an average grade of 700 ppm Mo (Clark and Baudry, 2011).

3.3. Hydrothermal alteration

Seven types of alteration – i.e., potassic, phyllic, sericitic, argillic, propylitic, and silicic alteration, as well as tourmalinization and greisenization – are observed in the area of the Zuun Mod deposit (Figs. 4, 5). Potassic, sericitic, and greisen alteration types occur to the south of the Zuun Mod porphyry system, while phyllic alteration occurs in wider areas surrounding the ore bodies within the porphyry system (Fig. 4). Tourmalinization occurs in the central part as well as to the west, mostly in association with silica alteration (Fig. 4), while silica alteration occurring southeast, north, and northeast is not associated with tourmalinization (Fig. 4). Argillic alteration mostly occurs to the north of the porphyry system (Fig. 4). These porphyry-related alteration types developed with zoning patterns mostly within the circular structure wherein the main porphyry Mo and Cu mineralization is associated with potassic alteration, while phyllic (QSP) and propylitic alterations were developed in its periphery. Argillic alteration and tourmalinization developed in the outermost part of the porphyry mineralization (Fig. 4).

Potassic alteration: Potassic alteration is represented by biotite + potassium feldspar + magnetite and is most strongly developed within the high-grade Mo (up to 9765 ppm) and Cu (up to 4370 ppm) zone that consists of intense stockwork ore within the quartz monzonite and granodiorite units (Figs. 5A, B). Potassium feldspar is frequent near the surface, with magnetite and biotite becoming increasingly more abundant at deeper levels.

Phyllic alteration: Phyllic alteration, characterized by quartz + pyrite + sericite, occurs within the andesite, granodiorite, and biotite granite units, facilitated by the formation of hydrothermal quartz veins (Figs. 4, 5C). The intensity of phyllic alteration increases to the north of the deposit while it decreases toward the northeast in accordance with the frequency of hydrothermal veins. The phyllic alteration is cogenetic with Cu-Mo mineralization with up to 100-2000 ppm Cu and 10-40 ppm Mo based on outcrop samples.

Sericitic alteration: Sericitization is represented by fine-grained sericite-quartz-pyrite that occur as alteration selvages of the quartz-pyrite veins and veinlets within the granodiorite in core samples from the Racetrack North orebody (Figs. 5D). Core assay data show that the sericite alteration is only rarely associated with the Mo mineralization.

Argillic alteration: Argillic alteration is developed in andesitic rocks that strike northwest. It is characterized by kaolinite, quartz, sericite, and lesser hematite (Figs. 5E, F). The argillic alteration transitions to phyllic alteration toward the Racetrack South and

Stockwork orebodies to the south. Outcrop samples contain up to 150 ppm Cu and 10 ppm Mo.

Propylitic alteration: Propylitic alteration is represented by chlorite-carbonate-epidote assemblages within andesite. The alteration forms a zone of ca. 2000 m in length and 300 m in width to the north of the deposit (Fig. 4) that likely developed during the emplacement of the monzonite and granodiorite into the andesite (Fig. 5G). Surface and drill core samples with propylitic alteration contain negligible Mo and Cu contents (i.e., 10 ppm Cu and 1 ppm Mo), which indicates that the Mo and Cu mineralization is not associated with the propylitic alteration.

Silica alteration: Silica alteration occurs variably, depending on the local composition and structure of the granitoids (Fig. 4). Silicic alteration is closely associated with phyllic alteration and characterized by quartz-sericite-pyrite with quartz being the dominant mineral (Fig. 5H). Outcropping silicified rock samples contain up to 100-200 ppm Cu and 100-300 ppm Mo.

Tourmalinization: Tourmalinization occurs within the volcanic unit, located approximately 1.3 km northwest of the Zuun Mod deposit. The tourmalinization zone is discontinuously 2.2 km long and 450 m wide and associated with strong silicification (Fig. 4). The tourmaline is fine-grained, smeared with irregular and radiating textures (Fig. 5I). The rock chip geochemical data suggest that there is no systematic relationship between tourmaline and Cu-Mo mineralization.

Greisen alteration: Greisen alteration is restricted to the southeast part of the Zuun Mod deposit at the contact between the quartz syenite and quartz monzonite units at the surface (Figs. 4, 5J). The alteration zone is approximately 250 m long and 50 m wide and characterized by abundant muscovite, sericite, and quartz which are associated with iron oxide/hydroxide minerals such as hematite and limonite. Rock chip geochemical data show that the greisen alteration zone contains 100-150 ppm Cu and 10-20 ppm Mo, indicating that the greisen alteration may be related to the Mo mineralization in the Zuun Mod deposit area.

4. Methods

4.1. Samples and sample preparation

Samples for mineralogical, lithogeochemical, and geochronological analyses of the granitoids and stockwork veins from the Zuun Mod porphyry Mo-Cu deposit were collected from nine drill holes and outcrops which are shown in Figure 2. Sample locations and modes of sampling, as well as an overview on what kind of analyses were carried out, are provided in Appendix 1. Ten thin sections were prepared at the School of Geology and Mining Engineering, Mongolian University of Science and Technology (MUST) to characterize the granitoids that are spatially associated with the Mo and Cu mineralization. Nine polished blocks were prepared at MUST to characterize the ore mineral assemblages and crystallization sequences. Microscopic studies under transmitted- and reflected-lights were conducted using a Nikon Eclipse 100 microscope at MUST.

Two least weathered and visually altered samples with weights of 300 and 600 g were taken from the drill cores (ZMD-113-150 and ZMD-29-182.1) for zircon U-Pb geochronology. Additionally, one drill core sample (ZMD-10-352) was selected for molybdenite Re-Os geochronological analysis. Zircon grains were separated in the laboratory of the Center for Research and Innovation in Technology Minerals at MUST before being mounted in epoxy resin and polished at the laboratory of the Guangzhou Institute of Geochemistry, Chinese Academy of Sciences, China, following the protocol described in Boldbaatar et al. (2019). Cathodoluminescence (CL) images of zircon grains were taken using a JEOL JXA-8100 scanning electron microscope equipped with an energy-dispersive spectroscope and Mono CL3 detector (Gatan) at the Guangzhou Institute of Geochemistry. Molybdenite grains from quartz vein were prepared in the laboratory of the Center for Research and Innovation in Technology Minerals. Molybdenite grains were handpicked under a binocular microscope after the sample was crushed, washed in distilled water, and heavy mineral concentrates were magnetically separated.

4.2. U-Pb geochronology

Zircon U-Pb age dating analysis was carried out using an Agilent 7500cx quadrupole laser ablation inductively coupled plasma mass spectrometer (LA-ICP-MS) connected to a Resonetic 193 nm ArF excimer laser ablation system at the Guangzhou Institute of Geochemistry following the analytical procedure and operating conditions described in Yuan et al. (2004). Target areas for U–Pb geochronological analysis were selected within transparent, relatively automorphic, and zoned magmatic grains (14 and 15 grains) without any cracks or inclusions. Isotope data were acquired using a static mode with laser diameter of 30 μm. The laser-induced elemental fractionation and instrumental mass bias were corrected against the Temora and NIST SRM 610 zircon standards where the measurements on zircons were bracketed by the analyses on NIST SRM 610 and Temora zircons (Black et al., 2003; Gao et al., 2002; Paces and Miller Jr., 1993). Data reductions and calculations of isotopic ratios were performed using GLITTER (Griffin et al., 2008). Errors were estimated by propagating numerical errors (Ludwig, 2003; 1980) with uncertainties for individual analyses (ratios and ages) falling within the 2σ level, whereas uncertainties for the weighted mean ages are reported at 95% confidence levels. The NIST SRM 610 analyses show that the deviations from certified values are < 0.006% and external precisions are < 1.6% (Table A.1). The Temora standard shows greater accuracy and precision due to the heterogenous distribution of U, Th, and Pb (Table A.1). Concordia diagrams, relative probability plots with stacked histograms of the radiogenic $^{206}Pb/^{238}U$ ages, and weighted mean calculations were generated using Isoplot 3.0 (Ludwig, 2003).

4.3. Re-Os molybdenite geochronology

Ultra-pure molybdenite grains with 5 gr separated from quartz vein hosted in quartz monzonite were analyzed for Re-Os analysis using a TJA PQ ExCELL ICP-MS in the Re-Os Laboratory, National Research Center for Geoanalysis, Chinese Academy of Geological Sciences in Beijing, China. The molybdenite concentrates were digested using Carius tube digestion, following the analytical procedures described in Shirey and Walker (1995) and Du et al. (2001); Du et al. (2004). Molybdenite model ages were calculated using an equation $^{187}Os_m = {}^{187}Re_m \times (e^{\lambda t} - 1)$ with the assumption of no initial radiogenic ^{187}Os, wherein m is measured, t is time, and λ is a ^{187}Re decay constant of 1.666×10^{-11} per year (Smoliar et al., 1996). To test analytical accuracy, molybdenite standard HLP, sourced from a carbonate vein-type Mo-Pb deposit in the Jinduicheng-Huanglongpu area of Shaanxi province, China was analyzed (Stein et al., 1997). The accuracy falls within 0.7% of the standard measurements (Table A.2-2). The results are reported with 0.5% error, which is a conservative estimate and reflects all sources of errors. Average blanks for the total Carius tube procedure yielded ca. 0.3 pg Re and 0.03 pg Os (Table A.2-1).

4.4. Whole-rock analysis

A total of eleven samples were commercially analyzed for their whole-rock major, minor, and trace elements chemistry at ALS Canada Ltd. Major and minor elements were analyzed using inductively coupled plasma atomic emission spectroscopy (ICP-AES), while trace elements were analyzed using solution ICP-MS. Standard samples of AMISO 167 and SY-4 were analyzed for ICP-AES and OREAS 146 and SY-4 were analyzed for ICP-MS methods wherein the major and minor elements fell within an accuracy of ± 8% and an external precision of ±25% (2-sigma; Table A.3). The trace elements fell within an accuracy of ± 15% and an external precision of ±30% (2-sigma; Table A.3). For duplicate analyses, the precision fell within ±15% (2-sigma; Table A.3).

5. Results

5.1. Petrography

The granitoids included in this study are fine- to medium-grained quartz monzonite, biotite granodiorite, and biotite granite with seriate textures (Fig. 6). The quartz monzonite (samples ZMD113, KKMD-03 299.4 m, and ZMD-12 204.5 m) contains plagioclase (30-35 modal %), potassium feldspar (30-35 modal %), hornblende (15-20 modal %), biotite (10-15 modal %), quartz (10-15 modal %), and accessory zircon, sphene, chalcopyrite, pyrite, and magnetite (Figs. 6A, B, C). Plagioclase forms prismatic grains 0.8-2.1 mm in the longest direction and shows polysynthetic twinning as well as locally weak compositional zonation in transmitted light (Figs. 6A, C). The central part of the plagioclase is affected by clay and sericitic alteration (Figs. 6A, B, C). Anhedral grains of potassium feldspar and quartz occur between plagioclase grains. Potassium feldspars are 0.4-1.6 mm in the longest direction and show perthite growth while quartz grains are 0.3-1.0 mm in the longest direction (Figs. 6A, B). Hornblende shows euhedral to subhedral textures with sizes up to 1 mm in the longest direction and is locally replaced by chlorite (Figs. 6A, B). Biotite grains display euhedral to anhedral textures with sizes between 0.2-0.5 mm in the longest direction and are partially replaced by chlorite and locally contain small epidote grains (Figs. 6B, C). Accessory ore minerals such as chalcopyrite, pyrite, and magnetite are found (Fig. 6B). Accessory sphene (Figs. 6B, C) and zircon grains were found as well.

The biotite granodiorite (samples ZMD-39 112 m, ZM02, ZMD-16 182, FS-48, and FS-56) consists of plagioclase (40-45 modal %), potassium feldspar (20-25 modal %), quartz (20-25 modal %), biotite (15-20 modal %), hornblende (up to 5 modal %), and accessory zircon and ore minerals such as magnetite, pyrite, chalcopyrite, bornite, covellite, and molybdenite (Figs. 6D, E, F). The plagioclase grains show prismatic, euhedral to subhedral, and polysynthetic textures with minor alteration to clay and sericite. Locally, some of the plagioclase grains show compositional zonation in transmitted light (Figs. 6D, E). The size of the plagioclase varies between 0.5 and 3.3 mm in the longest direction. Based on an inclination angle between 15° and 17°, it is defined as andesine with $An_{30} - An_{32}$ (Milam et al., 2010). Potassium feldspars show anhedral and perthitic textures with sizes between 1.3-

3.5 mm in the longest direction and are irregularly altered to clay (Figs. 6D, F). Some of the potassium feldspar grains enclose plagioclase while others are locally replaced by quartz (Fig. 6E). Quartz displays an anhedral texture with sizes between 0.3 and 2.3 mm in the longest direction and locally encloses plagioclase (Figs. 6D, E, F). Biotite with euhedral to anhedral textures has sizes varying from 1.2 to 2.6 mm in the longest direction and is partially replaced by chlorite and secondary biotite (Figs. 6E, F). Hornblende is prismatic in shape with a size of 0.6-1.5 mm and shows less alteration compared to biotite (Fig. 6F). The biotite granodiorite also contains accessory of magnetite, pyrite, molybdenite, and copper sulfides (Fig. 6E). Ore minerals with sizes between 0.4-2.1 mm are mainly associated with biotite flakes (Fig. 6E).

The biotite granite (samples ZMD-05 350.5-350.6 m, and FS55) contains quartz (35-40 modal %), plagioclase (25-30 modal %), potassium feldspar (20-25 modal %), biotite (15-20 modal %), hornblende (0-5 modal %), and accessory zircon, sphene, magnetite, pyrite, chalcopyrite, molybdenite, and sphalerite (Figs. 6G, H, I). Quartz grains are anhedral with sizes between 0.3-3.8 mm and usually fill open spaces between other minerals (Figs. 6G, H, I). Plagioclase mainly occurs as prismatic crystals with polysynthetic twinning and locally compositional zoning observed in transmitted light (Figs. 6G, H). Grain sizes vary between 1.5-3.2 mm in the longest direction and the grains are partially altered to clay and sericite (Fig. 6H). Plagioclase grains with polysynthetic twinning show 13-15î extinction, indicating they are An_{26} - An_{28} oligoclase in composition (Milam et al., 2010). Potassium feldspar shows an anhedral texture with sizes of 2-4 mm in the longest direction (Figs. 6G, H, I). Biotite with subhedral blades is between 0.5-1.5 mm in size, and partially altered to chlorite and/or replaced by secondary biotite (Figs. 6G, H). Hornblende grains are euhedral to subhedral with sizes between 0.5-2.3 mm. Accessory zircon occurs as inclusions in biotite as well as between grains, while magnetite and pyrite occur by replacing biotite and/or are intergrown with secondary biotite.

5.2. Ore mineralogy

Ore minerals found in the Zuun Mod porphyry Mo-Cu deposit include molybdenite, chalcopyrite, pyrite, magnetite and rare bornite, covellite, chalcocite, specularite, and sphalerite. The ore minerals generally occur as fine to coarse grains disseminated in the intrusive rocks. In stockwork and sheeted quartz veins, ore minerals occur as fine to coarse clots, as well as thin bands along vein contacts (Fig. 7). Molybdenite and chalcopyrite represent the most abundant ore minerals in the Zuun Mod deposit. Based on petrographic observations, Mo and Cu mineralization can be grouped into five main assemblages: 1. Quartz monzonite-hosted pyrite±chalcopyrite±molybdenite assemblages (Figs. 7A, B, C); 2. Granodiorite-hosted pyrite±chalcopyrite±molybdenite±magnetite±bornite±covellite assemblages (Figs. 7D, E, F); 3. Biotite granite-hosted pyrite±chalcopyrite±molybdenite assemblages (Fig. 7G), 4. Quartz vein-hosted magnetite±chalcopyrite±molybdenite, pyrite, and rare sphalerite and chalcocite assemblages (Figs. 7H, I). The main Mo-mineralized stages are quartz-molybdenite and quartz-chalcopyrite-molybdenite veins.

Quartz monzonite-hosted pyrite±chalcopyrite±molybdenite assemblages: Ore minerals within the fine- to medium-grained quartz monzonite show fine to coarse disseminated textures. Pyrite is coarse (up to 3 mm) and forms cubic crystals and some grains locally contain small (0.4 mm) subhedral chalcopyrite grains (Fig. 7A). Chalcopyrite shows a range of forms from prismatic isometric to irregular shapes with sizes up to 1.2 mm (Figs. 7A, B). Molybdenite forms aggregates of elongated flakes with a length up to 1.2 mm individually that often occurs filling open spaces and fractures, as well as by replacing biotite and is intergrown with secondary biotite and magnetite (Figs. 7B, C).

Granodiorite-hosted pyrite±chalcopyrite±molybdenite±magnetite±bornite±covellite assemblages: Within granodiorite, molybdenite forms aggregates with elongated grains (up to 0.5 mm in length individually), which mainly occur along the fractures of the rock (Fig. 7D). Anhedral and subhedral grains of pyrite (up to 2.4 mm) are mainly associated with biotite and locally contain chalcopyrite (Fig. 7D). Chalcopyrite occurs as irregular in shape and up to 1.6 mm in the longest direction filling interstitial spaces between quartz, biotite, pyrite, and molybdenite (Figs. 7D, E) and is partly replaced by secondary covellite (Fig. 7F). Bornite occurs as an overgrowth rimming chalcopyrite (Fig. 7F).

Biotite granite-hosted pyrite±chalcopyrite±molybdenite assemblages: Ore minerals that occur within the fine- to medium-grained biotite granite show disseminated texture and formed along small veinlets. Within the biotite granite, chalcopyrite forms anhedral grains with sizes up to 1.5 mm in the longest direction (Fig. 7G). Molybdenite has sizes up to 1.2 mm (Fig. 7G).

Quartz vein-hosted magnetite-chalcopyrite-molybdenite, pyrite, and rare sphalerite and chalcocite assemblages: Chalcopyrite and molybdenite are the dominant ore minerals in the quartz veins. Chalcopyrite forms anhedral grains with sizes up to 1 mm in the longest direction (Fig. 7H). Molybdenite forms elongated grains up to 1 mm in length and their batches (Figs. 7H, I). Irregularly shaped magnetite (0.6 mm) and sphalerite (0.4 mm) occur along the quartz veins together with chalcopyrite (Fig. 7H).

5.3. Zircon U-Pb geochronology

Two new U-Pb ages for magmatic zircons have been determined to constrain magmatic events at the Zuun Mod porphyry Mo-Cu deposit. Zircon CL images are given in Figure 8. Concordia and weighted mean ages are illustrated in Figure 9. All isotopic ratios are given in Table 1. Zircon grains separated from the granitoids are colorless, clear, idiomorphic, prismatic under binocular microscope, and 100-200 um in the longest direction (Fig. 8). Obvious inherited cores were not analyzed in this study.

Sample ZM113. The Th/U ratios range between 0.25 and 1.42 (Table 1). Zircon U-Pb age results were acquired from 14 grains with ages varying from 324.7 Ma to 293.1 Ma; the Concordia age of the 14 measurements is constrained to be 305.3 ± 3.6 Ma, MSWD = 0.97, weighted average age 305.3 ± 4.4 Ma, MSWD = 2.4 (Figs. 9A, B).

Sample ZM02. The Th/U ratios range from 0.37 to 0.89 (Table 1). Zircon U-Pb age data were obtained from 15 grains with ages ranging from 309.0 Ma to 296.5 Ma; the Concordia age is constrained as 301.8 ± 2.7 Ma, MSWD = 0.47 and the weighted average age as 301.7 ± 2.6 Ma, MSWD = 0.4 (Figs. 9C, D).

5.4. Re-Os geochronology

The results of two Re-Os runs of ultrapure molybdenite concentrates are provided in Table 2. The concentrations of total Re are 155.3 and 160.3 ppm, while the total contents of ^{187}Os are 481.9 and 502.1 ppb. The obtained ages are 295.6±4.8 Ma and 298.4±4.9 Ma (2σ) and thus within analytical uncertainty of one another.

5.5. Whole-rock geochemistry

The chemical compositions of the Bayanbulag intrusive complex are given in Table 3. The granitoid rocks in this study are identified as quartz monzonite, granodiorite, and granite on the basis of the total alkalis versus silica diagram (Fig. 10A; Middlemost 1994), with characteristics of calc-alkaline to high-K calc-alkaline series rocks (Figs. 10B, C; Irvine and Baragar, 1971; Peccerillo and Taylor, 1976). The rocks further display metaluminous to slightly peraluminous signatures with A/CNK ratios from 0.9 to 1.3 (Fig. 10D; Middlemost, 1994). On the tectonic discrimination diagram of Ta vs. Yb after Pearce et al. (1984), the granitoids plot in the volcanic arc field (Fig. 10E). On the SiO_2 vs. Rb/Zr (Fig. 10F) and Rb/30-Hf-Ta*3 diagrams (Fig. 10G) that distinguish granitoids emplaced in a post-collisional setting from those emplaced in a volcanic-arc setting, after Harris et al. (1986), the granitoids of the Bayanbulag complex plot in the late- and post-collisional field. The granitoids also have adakitic features based on their Sr/Y ratios (Fig. 11A) following the classification of Richards and Kerrich (2007) and fertile magma features based on their Sr/Y vs. SiO_2 ratios (Fig. 11B; Loucks, 2014).

An Y vs. SiO_2 diagram (Fig. 12A) shows that the granitoids formed through amphibole-bearing fractionation (Koprubasi and Aldanmaz, 2004), while a Dy/Yb vs. SiO_2 diagram (Fig. 12B) shows both amphibole and garnet fractionation occurred (Davidson et al., 2007). C1 chondrite-normalized rare earth element (REE) patterns show that the granitoids are characterized by an enrichment in light REE (LREE) relative to heavy REE (HREE) without consistent negative Eu anomalies (Fig. 13A). Bulk Silicate Earth-normalized patterns indicate that all samples are enriched in fluid-soluble elements including large ion lithophile elements (LILE: Rb, K, Ba, Sr), Pb, and U, but depleted in some high field strength elements (HFSE) such as Nb, Ta and Ti (Fig. 13B).

6. Discussion

Despite being the largest deposit in the Edren terrane in Southwest Mongolia, the Bayanbulag intrusive complex hosting the Zuun Mod Mo-Cu porphyry deposit remains to be fully understood with respect to geochemical signatures and tectonic environment. Studies on its genesis and classification are only limited to technical reports in which the deposit classification is still controversial. Whereas Gillis (2007) suggested a British Columbia (BC) type or Endako-type origin, Taylor et al. (2012) described the deposit as a possibly arc-related porphyry Mo deposit. Alternatively, Clark and Baudry (2011) proposed a transitional style between Endako and Climax types.

The goals of this study are to (i) better characterize the mineralization style at the Zuun Mod deposit through a lithogeochemical study of the granitoid rocks that host the Mo and Cu mineralization as well as through new petrographic observations of the granitoids and ore zones; and (ii) to constrain the timing of events that led to the formation of the deposit. The data are used to propose an ore genetic model and to reflect on the geodynamic evolution that facilitated the formation of the Zuun Mod deposit.

6.1. Tectono-magmatic evolution of the Bayanbulag intrusive complex

The composition of the granitoid rocks studied here allows for novel insight into the source region of the Bayanbulag intrusive complex and the regional geodynamic evolution that facilitated the formation of the Zuun Mod Mo-Cu porphyry deposit. It is noted that the possible elemental mobility needs to be evaluated before discussing the tectono-magmatic evolution based on lithogeochemical data. The loss on ignition (LOI) values of these granitoids range from 0.6 to 2.19 wt % (except one value of 3.13 wt %) while the petrographic observations indicate minor potassic, clay, and chloritic alteration types represented by secondary biotite, sericite in plagioclase, and chlorite in biotite, respectively (Fig. 6). Potassic alteration should result in loss of Na_2O, Sr, and Ba while gain of K_2O and Rb; however, linear trends between these elements are not observed (Fig. A2). Additionally, replacement of plagioclase by sericite should result in loss of Na_2O and Sr, but gain of K_2O, LOI, and Rb and such trends are not observed (Fig. A2). Based on these features, it can be assumed that minor hydrothermal alterations observed in petrographic observations did not mobilize major and mobile elements and therefore, the lithogeochemical data can be used for further evaluations (Tang et al., 2022).

As illustrated in Figure 10, the rocks of the Bayanbulag intrusive complex are quartz monzonites, granodiorites, and granites with I-type, metaluminous to slightly peraluminous, and calc-alkaline to high-K calc-alkaline affinities that were emplaced in a post-collisional setting. The lack of a negative Eu anomaly (Fig. 13A) is indicative of a hydrous magma, wherein plagioclase fractionation was subdued due to abundant water content (Loucks, 2014; Müntener et al., 2001). A hydrous magma composition is petrographically supported by the presence of abundant biotite and lesser hornblende in the petrographic studies (Fig. 6; Johnson et al., 1991; Merzbacher and Eggler, 1984; Richards, 2011). The enrichment in LILE and negative trough of Nb, Ta, and Ti (Fig. 13B) indicates a magma sourced from asthenospheric mantle metasomatized by slab-derived fluids may have been involved for generation of the granitoids (Richards, 2003; Sillitoe, 2010; Tatsumi et al., 1986). Based on these geochemical signatures, it can be inferred that the Bayanbulag intrusive complex was sourced from previously subduction-modified lithosphere in a post-collisional setting as the postsubduction magmas share similar geochemical signatures with precursor arc magmas (Richards, 2009, 2015). It is noted that similar geochemical signatures were demonstrated in porphyry Cu-Mo deposits formed in a post-collisional setting such as the Qulong, Bairong, and Chongjiang porphyry Cu-Mo deposits in the Gangdese porphyry Cu belt (Li et al., 2011).

It is noted that the presence of biotite, hornblende, and sphene has resulted in a peraluminous affinity of these granitoids up to ~1.3 (Fig. 10D; Chappell and White, 2001). Such high A/CNK values generally imply a sedimentary source and/or assimilation of sedimentary rocks upon pluton emplacement (Chappell and White, 2001). However, the peraluminous affinity is not restricted to only a sedimentary source and/or assimilation of sedimentary rocks, but it also may reflect fractional crystallization of typical mantle wedge-derived picrobasaltic melts (Müntener and Ulmer, 2006; Pettke et al., 2010) and/or partial melting of metaluminous crustal source (Chappell et al., 2012). Such peraluminous affinity further supports our findings that the Bayanbulag intrusive complex was emplaced in a post-collisional setting. Because partial remelting of a subduction-modified lithosphere with preceding mantle-wedge derived basaltic magma and/or hydrous cumulate zones of precursor arc (Richards, 2009) and/or with thickened mafic lower crust formed by underplating of mantle-derived mafic magmas (Hou et al., 2011) are often suggested as a magma source for the formation of post-collisional porphyry deposits.

Magmas with calc-alkaline affinities dominate in mature continental arcs and post-collisional zones as opposed to tholeiites that dominate in immature island arcs and nascent continental arcs (Hildreth and Moorbath, 1988; Richards, 2015; Richards et al., 2012). The origin of calc-alkaline signatures is still controversial whether the signature: (1) originates from a mantle wedge (Carmichael, 1991); (2) develops through magma fractionation (Audétat, 2010; Soesoo, 2000); or (3) forms through contamination and mixing with Si-rich and Fe-poor crustal materials while ascending (Hoshino et al., 2016). The broadly accepted hypothesis is that calc-alkaline magmas are sourced from the metasomatized mantle wedge and form through early fractionation of Fe-rich minerals such as magnetite, amphibole and garnet (Sisson and Grove, 1993; Tang et al., 2018) due to high water contents in a mature arc setting (Richards, 2003; Richards et al., 2012). Additionally, partial melting of the previously subduction-modified lithosphere and juvenile lower crust share many similarities with respect to geochemical signatures with the arc magmas, and therefore, have calc-alkaline to mildly alkaline character (Richards, 2009, 2015). The fact that the formation of Zuun Mod is spatiotemporally associated with the calc-alkaline to high-K calc-alkaline granitoids of the Bayanbulag complex implies that the host granitoids are the most extreme representative of these calc-alkalic differentiation trend (Loucks, 2014) and formed in a thickened crust because calc-alkalinity of magma is linearly correlated with crust thickness (Chiaradia, 2014). Geochemical signatures indicative of a post-collisional setting (Figs. 10E, F), as well as amphibole and garnet fractionation trends (Fig. 12), support a thickened continental crust that likely formed as a result of the collision (Chin et al., 2018). Underneath the thickened continental crust during post-collision, calc-alkaline to high-K calc-alkaline magma derived from subduction-modified lithosphere has similar geochemical characteristics to those of volcanic-arc magma (Harris et al., 1986).

For the formation of porphyry-type deposits, a high Sr/Y ratio has been proposed as an important magma fertility criterion (Chiaradia and Caricchi, 2017; Chiaradia et al., 2012; Richards and Kerrich, 2007). However, the origin of high Sr/Y signatures (i.e., adakitic signatures) in magmas still remains debated. For example, Defant and Drummond (1990) and Martin et al. (2005) suggest that high Sr/Y ratios are indicative of slab melting, whereas Petford and Gallagher (2001) and Zellmer et al. (2012) suggest partial melting of the lower crust. Growing evidence suggests that magma with high Sr/Y ratios forms due to early hornblende and garnet fractionation and delayed plagioclase production in response to higher dissolved water contents with possible involvement of crustal melting and assimilation (Chiaradia et al., 2012). In this instance, high Sr/Y ratios result from early fractionation of Y into hornblende and/or garnet and Sr concentrations in a residual magma due to the instability of plagioclase, the main host of Sr (Alonso-Perez et al., 2009; Drake and Weill, 1975). Chiaradia and Caricchi (2017) demonstrated through stochastic modelling that the causative magmas of giant porphyry deposits have Sr/Y ratios between 50 and 150. Out of 11 samples included in this study, 10 are characterized by Sr/Y ratios ranging between 50 and 150 (Fig. 11A) and thus fall within the area characterized by fertile magmas (Fig. 11B). These adakitic fertile signatures must have derived from partial remelting of subduction-modified lithosphere which was fertilized by preceding arc magmatism and subsequent amphibole and garnet fractionation in a post-collisional setting such as those in the Gangdese porphyry Cu belt wherein porphyry-related adakites are often hosts to giant porphyry Cu-Mo deposits (Li et al., 2011).

Based on the lithogeochemical signatures of the Bayanbulag intrusive complex, we argue that the granitoids that facilitated the formation of the Zuun Mod porphyry Mo-Cu deposit was emplaced in a post-collisional setting and was sourced from a subduction-modified lithosphere which has been fertilized by preceding arc magmatism. Detailed geological and tectonic history of the Edren terrane will be discussed in section 6.4.

6.2. Revised classification of the Zuun Mod deposit

Molybdenum porphyry-type deposits are commonly classified either as Climax-type deposits with high F contents related to within-plate, highly evolved A-type granitic magmatism (Audétat and Li, 2017; Ludington and Plumlee, 2009), or as Endako-type deposits which are associated with arc-related I-type magmatism and fluorine-poor granitoids (Ludington et al., 2009; Taylor et al., 2012; Westra and Keith, 1981). The granitoids that host the Zuun Mod deposit are I-type rocks that were emplaced in a post-collisional environment

(Figs. 10E, F), indicating that Zuun Mod cannot be classified as a Climax-type deposit. This hypothesis is supported by the observation that the granitoids plot outside of the within-plate granite field commonly associated with Climax-type deposits (Fig. 10F). Although Clark and Baudry (2011) noted the presence of fluorite with up to 5-14% in samples from drill hole KKMD03, and thus interpreted the origin of the deposit as a transitional style between the Climax and Endako types, no fluorite was observed in the samples we studied. Additionally, the granitoids with values of Nb < 12 ppm and Rb < 110 ppm at Zuun Mod are not highly fractionated which strengthens the argument that the deposit should not be classified as a Climax type deposit, as they are commonly characterized by Nb > 50 ppm and Rb > 500 ppm (Ludington and Plumlee, 2009). Low-F Endako-type deposits form in an arc environment and are characterized by Rb < 300 ppm and Nb < 30 ppm (Taylor et al., 2012). The geochemical signatures pointing to the formation of the Zuun Mod porphyry Mo-Cu deposits in a post-collisional environment rule out the possibility of being an Endako-type deposit (Taylor et al., 2012). Based on these geochemical features of host rocks, we argue that the Zuun Mod deposit should be reclassified as a Mo-rich porphyry Cu deposit. Further discussion for this classification is provided in section 6.4.

6.3. Timing of intrusion emplacement and Mo-Cu mineralization

The zircon grains collected from representative quartz monzonite and granodiorite yield U-Pb ages of 305.3±3.6 Ma and 301.8±2.7 Ma, respectively (Fig. 9). Within the quartz monzonite and granodiorite, the zircon Th/U ratios range from 0.25 to 1.42, implying a magmatic origin for the analyzed zircon spots as opposed to metamorphic zircons, which normally have Th/U ratios less than 0.01 (Hoskin and Schaltegger, 2003). A magmatic origin for the analyzed zircon grains is also supported by the oscillatory zonation observed under CL analyses (Fig. 8; Hoskin and Schaltegger, 2003). Additionally, the presence of oscillatory zonation indicates that zircon inheritance or Pb loss has not affected the interpretation of the age of these samples (Corfu et al., 2003).

The Re-Os geochronometer in molybdenite is considered to be reliable in determining mineralization ages wherein the Re-Os ages are not easily disturbed by post-mineralization prolonged hydrothermal activities or metamorphic and/or tectonic events (Selby and Creaser, 2001; Stein et al., 1998). The mineralization age of the Zuun Mod deposit is defined at 297±4.8 Ma in average using molybdenite Re-Os geochronology (Table 3), which falls within the uncertainty of the emplacement age of the granodiorite determined as 301.8±2.7

Ma. Molybdenite flakes were collected from a B-type quartz vein with potassic selvages from the Stockwork orebody wherein the sulfide precipitation is suggested to have occurred during the early stages of magmatic-hydrothermal alterations (Klemm et al., 2007; Landtwing et al., 2005; Redmond et al., 2004; Richards, 2018).

The Re concentration within molybdenite ranges widely from < 10 ppm up to several wt % and is suggested to be controlled by the magma source and the degree of magma fractionation (Voudouris et al., 2013; Wu et al., 2017). Rhenium contents in molybdenite are the highest in magma sourced from mantle, decrease in magma that sourced from both mantle and lower continental crust, and are the lowest in magma sourced from crustal rocks (Wu et al., 2017). The average Re concentration within molybdenite at Zuun Mod is 158 ppm, higher than the Re concentrations identified within porphyry Mo and Mo-Cu type deposits found in China and elsewhere, as compiled by Zeng et al. (2014). The notably higher Re contents indicate a mantle source (Wu et al., 2017), which is in agreement with the lithogeochemical findings described above as subduction-modified lithosphere inherits preceding mantle-derived arc magma characteristics (Richards, 2009).

In summary, the new zircon U-Pb and molybdenite Re-Os ages presented in this study provide strong evidence for a late Carboniferous to early Permian magmatic event, and subsequent exsolution of magmatic-hydrothermal fluids were responsible for the formation of the Zuun Mod porphyry Mo-Cu deposit. The Re content within molybdenite supports the lithogeochemistry findings that the magma is sourced from subduction-modified lithosphere that inherited geochemical characteristics of preceding arc magma derived from metasomatized mantle wedge.

6.4. Geological model of the Zuun Mod deposit and regional implications

Based on the field and ore veins observations, as well as geochronological, lithogeochemical, and petrological studies of the granitoids that host the Zuun Mod porphyry Mo-Cu deposit, we propose a new geological model for the origin of the Zuun Mod deposit as illustrated in Figure 14. Here we note that the proposed model is based on the currently available data and is not necessarily to scale. The Zuun Mod Mo-Cu deposit formed from magmatic-hydrothermal fluids exsolved from the granodiorite and biotite granite of the Bayanbulag intrusive complex that intruded the quartz monzonite (Fig. 14). All the intrusive units of the Bayanbulag complex were emplaced into the early Carboniferous andesite and basaltic andesite of the Khuviinkhar Formation (Fig. 14). Petrographic and ore mineralogical observations indicate that magmatic-hydrothermal activities played significant roles in the Mo and Cu mineralization within the potassic alteration selvages in the quartz monzonite and granodiorite in addition to vein-hosted sulfide mineralization (Figs. 6, 7). The circulation of hydrothermal fluids caused the porphyry-style alteration types mapped within the circular structure (Fig. 4).

Within the circular structure, the Khuvyn Khar Cu-Ag occurrence was discovered at 2.2 km north of Zuun Mod (Fig. 2; Bat-Erdene, pers.commun, 2021). Drilling to test the geophysical target intersected 34 m of 1.3 wt % Cu and 9.2 g/t Ag at depths from 308 to 342 m (hole ZMD-121; Bat-Erdene, pers.commun, 2021). An unpublished geophysical survey suggests that the Zuun Mod and Khuvyn Khar porphyry deposits are located on both sides of a mushroom-shaped high resistivity and appear to have sourced from the same magma chamber beneath the andesite and basaltic andesite of the Khuviinkhar Formation (Fig. 14; Bat-Erdene, pers.commun, 2021). Therefore, we suggest that the Zuun Mod deposit is only the southern part of the entire porphyry Cu-Mo system, where Mo is the dominant component while Cu mineralization seems to be critical in the northwestern part of the system, possibly due to the decoupling feature of Mo and Cu (Spencer et al., 2015) which is common in porphyry Cu-Mo deposits such as Bingham (Seo et al., 2012) and El Teniente (Spencer et al., 2015).

The Bayanbulag regional scale fault (Fig. 1B) is interpreted to have formed due to dextral strike-slip movement based on unpublished regional RTP magnetic surveys and to have triggered a dilatational structure providing a favorable setting for the emplacement of the quartz monzonite, granodiorite and biotite granite at a shallow crustal level (Clark and Baudry, 2011; Gillis, 2007). The dextral strike-slip movement nearly parallel to the preceding arc subduction provided a favorable setting for the emplacement of an inferred batholith at mid-crustal level (Fig. 14; Richards, 2021; Tosdal and Richards, 2001). The dextral strike-slip movement likely contributed to the parallel openings in the host rocks to focus mineralized fluids forming sheeted quartz veins (Tosdal and Dilles, 2020), while stockwork veins formed from hydrofracturing from exsolution of mineralized fluids (Taylor et al., 2012).

In the Edren terrane (Fig. 2B), Devonian to Permian magmatic rocks exist, although precise age dating analyses are sparse. Nevertheless, the Edren terrane can be correlated with the Devonian-Carboniferous Dulate arc in eastern Junggar to the west (Hanžl et al., 2023). The sparse geochemical data show that the Devonian intrusive rocks (411 Ma and 359 Ma) are characterized by tholeiitic to calc-alkaline affinities indicative of an immature island arc environment (Togtokh et al., 2020; Tumurkhuu et al., 2010; Tumurkhuu et al., 2013). Carboniferous magmatic rocks, although a few of them have precise ages of 350 Ma, 335-330 Ma and 307 Ma, show calc-alkaline to high-K calc-alkaline affinities emplaced in a continental-arc setting (Tumurkhuu et al., 2010; Tumurkhuu et al., 2013; Hanžl et al., 2023). The early Permian granitoids with ages ranging from 294 Ma, 289±11 Ma to 273.8±4.2 Ma are A-type granitoids emplaced in a rift setting (Hanžl et al., 2023; Togtokh et al., 2020). Hanžl et al. (2023) correlated A-type granitoids that are distributed in the Dulate arc to the west, through the Edren terrane and the Khan Bogd alkaline complex (297-285 Ma) in the Gurvansayhan island arc terrane to the east as a narrow linear belt over 1600 km distance that were emplaced during Early Permian in a continental rift setting. In the eastern Junggar to the west, Zhang et al. (2018) demonstrated that subduction continued from ca. 355 Ma until 310 Ma which was followed by a continent-continent collision from 310-307 Ma and post-collisional magmatism from 307 to 265 Ma. Based on the age data of the granitoids distributed in the Edren terrane, we infer that the granitoids spatiotemporally associated with the Zuun Mod deposit formed in a post-collisional setting and were likely sourced from a subduction-modified lithospheric mantle and lower continental crust which was metasomatized by long-lasting subduction (Hou and Cook, 2009; Pettke et al., 2010). Subduction-modified lithosphere with extended prehistory is suggested to be an essential criterion for the formation of a Mo-rich porphyry Cu deposits as was the case for the formations of the Bingham porphyry Cu-Mo deposit in Utah, USA (Pettke et al., 2010) and world-class a Mo-rich porphyry Cu deposits in Gandese belt in the Tibetan orogen (Hou and Cook, 2009).

The Zuun Mod deposit formed as the result of an optimal alignment of processes starting from magma generation in the subcontinental lithospheric mantle to the emplacement of magma stocks in the upper crust within a favorable tectonic regime (Park et al., 2021). The fact that the Edren terrane is characterized by abundant porphyry and epithermal occurrences/deposits that are spatially and temporally associated with Carboniferous magmatic events makes the terrane an important exploration target. Specifically, the late Carboniferous magmatic events sourced from the subduction-modified lithosphere makes the terrane highly prospective for undiscovered porphyry systems. Additionally, the Edren terrane-wide dextral strike-slip movement along the Bayanbulag fault, i.e., transpressional regime, likely provided a favorable structural setting for porphyritic magma emplacement, further signifying its mineralizaton potential.

7. Conclusions

The Zuun Mod Mo-Cu porphyry deposit, despite being the first and largest deposit discovered in the Edren ensialic island arc terrane in Southwest Mongolia, is woefully understudied. Integrated petrographic, lithogeochemical, and geochronological studies as well as field and core observations reveal that molybdenite and chalcopyrite are the main ore minerals, with pyrite and magnetite that mostly occur within sheeted and stockwork quartz veins developed in quartz monzonite, granodiorite, and biotite granite which exhibit calk-alkaline to high-K calc-alkaline affinities and post-collisional trace element signatures. The ore minerals also occur as disseminated in the host rocks due to the breakdown of hornblende and biotite as a result of hydrothermal alterations. The LA–ICP-MS zircon U–Pb ages of granodiorite and quartz monzonite are 301.8 ± 2.7 Ma and 305.3 ± 3.6 Ma, respectively, and molybdenite Re–Os age is 297±4.8 Ma which indicates the mineralization age. The Zuun Mod deposit developed as a Mo-dominant branch while the Khuvyn Khar as the Cu-dominant branch from a hidden porphyry system at depth. The decoupling of Mo and Cu is probably due to the chemically evolving source and ore fluids that transported the metals and sulfur. The fact that late Carboniferous magmatic events appear to be fertile based on Sr/Y ratios, as well as the likelihood of sourcing from subduction-modified lithosphere and the wide distribution of Carboniferous magmatism in the Edren terrane together with other porphyry and epithermal type deposits/occurrences, altogether makes the terrane an important exploration target.

Ackowledgment

Authors are grateful for Erdene Resource Development Corporation's President, Chief Executive Officer Peter Akerley, Former Vice President Chris Cowan, Vice President Exploration Michael X, Gillis, and Senior Geologist Bat-Erdene Gendenjamts for their support and assistance in conducting research at the Zuun Mod deposit. Gankhuyag Altankhuyag also thanks Dr. Takeyuki Ogata for the help in conducting XRF and ICP-MS analyses at Akita University. Authors also thank the anonymous reviewers and their comments that only served to improve this manuscript. Lastly, authors greatly appreciate the Editor-in-Chief Dr. Mei-Fu Zhou and Associate Editor Dr. Ibrahim Uysal for handling the manuscript.

Author contributions

This research article is part of the first author's Ph.D. research. While working as a geologist for the Erdene Mongol LLC (branch company of Erdene Resource Development Corporation), Gankhuyag Altankhuyag collected the samples for the research. Gankhuyag Altankhuyag designed and composed the draft of this manuscript which was provided with feedback and improved by co-authors.

Funding

This research did not receive any specific grant from funding agencies in the public, commercial, or not-for-profit sectors.

Data availability

All data used for this study is presented in the figures, tables, and electronic appendix.

FIGURES

Fig. 1. A. Map of Mongolia showing island arc terranes and major/known porphyry-type deposits in South Mongolia, modified after Badarch et al. (2002). B. Simplified geological map of the Edren terrane and porphyry and epithermal deposits and occurrences, modified after Badarch et al. (1999).

Fig. 2. Simplified geological map of the Zuun Mod porphyry Mo-Cu deposit within an approximately circular structure, modified after Corey et al. (2006). Orebody boundaries for indicated and inferred resources estimation are illustrated (Gonchigjav et al., 2010). B. Geologic cross section A-A' of the Racetrack South orebody depicting crosscutting relationship of the Bayanbulag intrusive units and orebody boundary.

Fig. 3. The intrusive rock types found within the Zuun Mod porphyry Mo-Cu deposit area. A. Fine to coarse disseminated molybdenite mineralization associated with strongly potassic-altered quartz monzonite (sample ID: ZMD53 (142.1 m). B. Quartz-sulfide veins within the quartz monzonite (sample ID: ZMD59 (134.1 m)). C. Fracture-controlled molybdenite mineralization with minor pyrite (sample ID: ZMD11 (120-120.2 m)). D. Quartz-sulfide veins, disseminated molybdenite, chalcopyrite and pyrite mineralization associated with altered granodiorite (sample ID: ZMD70 (328 m)). E. Quartz-sulfide vein with potassic alteration halo within altered granodiorite (sample ID: ZMD29 (94 m)). F. Quartz-magnetite-

sulfide vein within potassic-altered granodiorite (sample ID: ZMD10 (345.7 m)). G. Disseminated fine to coarse molybdenite, chalcopyrite and pyrite mineralization associated with biotite granite (sample ID: ZMD70 (96 m)). H. Molybdenite-rich quartz stockwork with chalcopyrite and pyrite mineralization associated with biotite granite (sample ID: ZMD39, 244 m)). Abbreviations: Mo – molybdenite, Py – pyrite, Cpy – chalcopyrite, Qtz – quartz, Mag – magnetite.

Fig. 4. Alteration map of the Zuun Mod deposit area.

Fig. 5. The alteration types found within the Zuun Mod porphyry Mo-Cu deposit area. A. Quartz-calcite-magnetite-sulphide veins within altered potassic granodiorite (sample ID: ZMD10 (117.8 m)). B. Quarts-sulfide veins within potassic altered biotite granite (sample ID: ZMD57 (303.7-303.8 m)). C. Phyllic alteration characterized by quartz, pyrite, and sericite (sample ID: ZMD37 (285.3 m)). D. Centerline pyrite with sericitic alteration halo (sample ID: ZMD08 (135 m)). E. Argillic alteration with oxidized sulfide grains in an outcrop. F. Argillic alteration of plagioclase phenocrysts and magnetite veinlet (sample ID: KKMD10 (164 m)). G. Molybdenite-bearing quartz vein displaced by quartz veins with potassic alteration halos within granodiorite overprinting propylitic alteration (sample ID: ZMD71 (327.5 m)). H. Silicified zone within the granodiorite (sample ID ZMD 15, 252.5 m). I. Tourmalinization in dacite porphyry (sample ID: KKMD 02 (113.9 m)). J. the quartz-muscovite veins cuts the altered quartz syenite (outcrop sample). Mo – molybdenite, Py – pyrite, Cpy – chalcopyrite, Mag – magnetite, Qtz – Quartz, Ser – Sericite, Kaol – Kaolinite, Alun – Alunite, Tur – Tourmaline, Mus – Muscovite.

Fig. 6. Photomicrographs of representative transmitted-light images (all crossed polarizers) of the samples from the Zuun Mod porphyry Mo-Cu deposit. A. Quartz monzonite (sample ID: ZM113) with potassium feldspar and plagioclase partially altered by clay and sericite, and euhedral hornblende. B. Quartz monzonite (sample ID: KKMD-03 299.4 m) with plagioclase partially altered to clay and sericite, and sphene. C. Quartz monzonite (sample ID: ZMD-12 204.5 m) with zoned plagioclase partially altered to sericite and subhedral grains of sphene. D. Biotite granodiorite (sample ID: ZMD-39 112 m) with zoned plagioclase. E. Biotite granodiorite (sample ID: ZM02, ZMD-16 182 m) with zoned plagioclase and secondary biotite. F. Biotite granodiorite (sample ID: ZMD-16 182 m) zoned plagioclase, potassium feldspar, quartz, hornblende and chloritized biotite. G-H. Biotite granite (sample ID: ZMD-05 350.5-350.6 m) with prismatic and weakly zoned plagioclase and biotite partially replaced by

chlorite and secondary biotite. I. Biotite granite (sample ID: FS55) with subhedral potassium feldspar, plagioclase, quartz, and biotite. Abbreviations: Pl – plagioclase, Kfs – potassium feldspar, Bio – biotite, Hbl – hornblende, Qtz – quartz, Sph – sphene, Ep – epidote, Sec bio – secondary biotite, Mag – magnetite, Py – pyrite.

Fig. 7. Representative reflected-light photomicrographs of samples from the Zuun Mod porphyry Mo-Cu deposit. A-C. Quartz monzonite-hosted mineralization. A. Coarse pyrite crystals containing small chalcopyrite grains within quartz monzonite (Sample ID: ZMD113). B. Quartz monzonite-hosted molybdenite and chalcopyrite (Sample ID: ZMD12 (212.5 m)). C. Molybdenite batches and chalcopyrite within quartz monzonite (sample ID: ZMD12 (204.5 m)). D-F. Biotite granodiorite-hosted mineralization. D. Coarse anhedral crystal of chalcopyrite and molybdenite batches within granodiorite (sample ID: ZM02). E. Disseminated anhedral chalcopyrite within granodiorite (sample ID: ZMD16 (184.5 m)). F. Anhedral crystal of chalcopyrite within biotite granodiorite. Chalcopyrite crystals partially replaced by bornite and covellite (sample ID: KKMD-03 299.4 m). G. Biotite granite-hosted mineralization. Disseminated subhedral chalcopyrite crystals with minor molybdenite in biotite granite (Sample ID ZMD12 (202.5 m)). H-I. Quartz vein-hosted mineralization. H. Quartz sulphide vein within granodiorite porphyry (sample ID: ZMD16 (184.5 m)). I. B type quartz veinlet-hosted aggregate of molybdenite flakes and poikilitic chalcopyrite (sample ID: ZMD10). Abbreviations: Mo – molybdenite, Py – pyrite, Cpy – chalcopyrite, Mag – magnetite, Sph – Sphalerite, Bor – bornite, Cv – Covellite.

Fig. 8. Cathodoluminescence images of zircons with LA-ICP-MS spots and corresponding U-Pb ages. A. Quartz monzonite; B. Granodiorite.

Fig. 9. Concordant, histogram and weighted average plots of LA-ICP-MS zircon U-Pb analytical results. A-B. Quartz monzonite (sample ID: ZM113). C-D. Granodiorite (sample ID: ZM02 from drill hole ZMD-29-182.1 m). MSWD = mean square of weighted deviates.

Fig. 10. A. Classification of granitoids based on total alkalis vs. silica (Middlemost, 1994); B. AFM (A = Na_2O+K_2O, F = FeO_T, M = MgO) diagram showing tholeiitic vs. calc-alkaline trend, after Irvine and Baragar (1971); C. SiO_2 vs. K_2O discrimination diagram (Peccerillo and Taylor, 1976); D. A/CNK vs. A/NK discrimination diagram (Middlemost, 1994). Field boundary between I-type and S-type granitoids are from Chappell and White (1974); E. Ta vs. Yb tectonic discrimination diagram (Pearce et al., 1984); F. SiO_2 vs. Rb/Zr discrimination diagram (Harris et al., 1986). G. Rb/30-Hf-Ta*3 diagram, after Harris et al. (1986). VAG –

volcanic arc granitoids, WPG – within plate granitoids, syn-COLG – syn-collisional granitoids, LCG – late-collisional granitoids, PCG – post-collisional granitoids.

Fig. 11. A. Sr/Y vs. Y plot to show adakite after Richards and Kerrich (2007). B. Sr/Y vs. SiO_2 plot to show magma fertility after Loucks (2014).

Fig. 12. A. SiO_2 vs. Y plot to show fractionation trend after Koprubasi and Aldanmaz (2004). B. SiO_2 vs. Dy/Yb plot to show fractionation trend after Davidson et al. (2007).

Fig. 13. A. C1-chondrite-normalized spidergram; B. Bulk Silicate Earth-normalized spidergram. Normalization values are from McDonough and Sun (1995).

Fig. 14. The block diagram for the geological modeling of the Zuun Mod deposit area.

TABLES

Table 1. Isotopic data of U-Pb age determinations on zircon grains collected from the Bayanbulag intrusive complex.

Table 2. Re-Os isotope data for molybdenite sample from the Zuun Mod porphyry Mo-Cu deposit.

Table 3. Whole-rock geochemical data for the host granitoids of the Zuun Mod porphyry Mo-Cu deposit in Southwest Mongolia.

APPENDIX

Table A1. Samples included in this study with drillhole ID, depth, lithology, orebody, and analyses carried out.

Fig. A2. Binary plots illustrating affects of hydrothermal alterations. A. Na2O vs. LOI; B. K2O vs. LOI; C. CaO vs. LOI; D. MgO vs. LOI; E. Fe2O3 vs. LOI; F. Al2O3 vs. LOI; G. Rb vs. LOI; H. Sr vs. LOI; I. Ba vs. LOI.

Table A3-1. Blank measurements.

Table A3-2. Measuremen on the Standard GBW04435 (HLP).

Table A3-3. Certified values (Stein et al., 1997).

Table A4. Accuracy and precision calculations of the standard and dublicate measurements of whole-rock geochemical data.

References:

Alonso-Perez, R., Müntener, O., Ulmer, P., 2009. Igneous garnet and amphibole fractionation in the roots of island arcs: experimental constraints on andesitic liquids. Contributions to Mineralogy and Petrology 157, 541-558.

Altankhuyag, G., 2008. The annual exploration report for Zuun mod area (license number 4476X) in 2007, Shinejinst soum, Bayankhongor province, Ulaanbaatar, Mongolia (in Mongolian).

Audétat, A., 2010. Source and evolution of molybdenum in the porphyry Mo(–Nb) deposit at Cave Peak, Texas. Journal of Petrology 51, 1739-1760.

Audétat, A., Li, W., 2017. The genesis of Climax-type porphyry Mo deposits: Insights from fluid inclusions and melt inclusions. Ore Geology Reviews 88, 436-460.

Badarch, G., Dickson Cunningham, W., Windley, B.F., 2002. A new terrane subdivision for Mongolia: Implications for the Phanerozoic crustal growth of Central Asia. Journal of Asian Earth Sciences 21, 87-110.

Badarch, G., Makhbadar, T., Orolmaa, D., Khosbayar, P., Tumurtogoo, O., 1999. Geology from Geological Map of Mongolia at scale 1:1000000. Institute of Geology and Mineral Resources, Academy of Sciences of the Mongolia. (in Mongolian).

Bat-Erdene, G., Altankhuyag, G., Molor, E., 2011. Geological setting and mineralization of the Zuun Mod porphyry Mo-Cu deposit. Mongolian Explorer 41, 84-100 (in Mongolian).

Black, L.P., Kamo, S.L., Allen, C.M., Aleinikoff, J.N., Davis, D.W., Korsch, R.J., Foudoulis, C., 2003. TEMORA 1: A new zircon standard for Phanerozoic U–Pb geochronology. Chemical Geology 200, 155-170.

Boldbaatar, E., Nanzad, B., Sereenen, J., Locmelis, M., Osanai, Y., Batsaikhan, N., Dashtseren, K., Zorigtbaatar, A., 2019. Geochronology and geochemistry of the intrusive suite associated with the Khatsavch porphyry Cu-Au (Mo) deposit, South Mongolia. Ore Geology Reviews 111, 102978.

Bukhbat, S., Naranbaatar, T., Badarch, G., Davaa, U., 1999. Report on geological mapping at a scale of 1:200000 in the area of Nemegt between 1996-1997, Ulaanbaatar, Mongolia (in Mongolian).

Carmichael, I.S.E., 1991. The redox states of basic and silicic magmas: a reflection of their source regions? Contributions to Mineralogy and Petrology 106, 129-141.

Chappell, B., White, A., 1974. Two contrasting granite types: Pacific Geology, v. 8.

Chappell, B.W., Bryant, C.J., Wyborn, D., 2012. Peraluminous I-type granites. Lithos 153, 142-153.

Chappell, B.W., White, A.J.R., 2001. Two contrasting granite types: 25 years later. Australian Journal of Earth Sciences 48, 489-499.

Chiaradia, M., 2014. Copper enrichment in arc magmas controlled by overriding plate thickness. Nature Geoscience 7, 43-46.

Chiaradia, M., Caricchi, L., 2017. Stochastic modelling of deep magmatic controls on porphyry copper deposit endowment. Scientific Reports 7, 44523.

Chiaradia, M., Ulianov, A., Kouzmanov, K., Beate, B., 2012. Why large porphyry Cu deposits like high Sr/Y magmas? Scientific Reports 2, 685.

Chin, E.J., Shimizu, K., Bybee, G.M., Erdman, M.E., 2018. On the development of the calc-alkaline and tholeiitic magma series: A deep crustal cumulate perspective. Earth and Planetary Science Letters 482, 277-287.

Clark, J., Baudry, P., 2011. Technical report on the Resource Estimate for the Zuun Mod project, Mongolia. Minarco mineconsult.

Corey, M.C., Altankhuyag, G., Enkhnasan, B., 2006. The annual exploration report for Zuun Mod area in 2005 (license number 4476X and 5131X), Shinejinst soum, Bayankhongor province, Ulaanbaatar, Mongolia (in Mongolian).

Corfu, F., Hanchar, J.M., Hoskin, P.W.O., Kinny, P., 2003. Atlas of Zircon Textures. Reviews in Mineralogy and Geochemistry 53, 469-500.

Davidson, J., Turner, S., Handley, H., Macpherson, C., Dosseto, A., 2007. Amphibole "sponge" in arc crust? Geology 35, 787-790.

Defant, M.J., Drummond, M.S., 1990. Derivation of some modern arc magmas by melting of young subducted lithosphere. Nature 347, 662-665.
Delgertsogt, B., Banzragch, B., Togtokh, J., Munkhzul, G., Ganbaatar, T., Lkhundev, S., 2014. The geology and metallogeny of the South-Western Mongolia. Mongolian Explorer 50, 23-33 (in Mongolian).
Dergunov, A.B., 2001. Tectonics, magmatism, and metallogeny of Mongolia, Routledge, London.
Dobretsov, N.L., Berzin, N.A., Buslov, M.M., 1995. Opening and tectonic evolution of the Paleo-Asian ocean. International Geology Review 37, 335-360.
Dobretsov, N.L., Buslov, M.M., Yu, U., 2004. Fragments of oceanic islands in accretion–collision areas of Gorny Altai and Salair, southern Siberia, Russia: Early stages of continental crustal growth of the Siberian continent in Vendian–Early Cambrian time. Journal of Asian Earth Sciences 23, 673-690.
Drake, M.J., Weill, D.F., 1975. Partition of Sr, Ba, Ca, Y, Eu2+, Eu3+, and other REE between plagioclase feldspar and magmatic liquid: an experimental study. Geochimica et Cosmochimica Acta 39, 689-712.
Du, A.D., Wang, S.X., Sun, D., Zhao, D., Liu, D., 2001. Precise Re-Os dating of molybdenite using Carius tube, NTIMS and ICPMS, In: Piestrzynski (Ed.), Mineral Deposits at the Beginning of the 21st century. CRC Press, pp. 405-407.
Du, A.D., Wu, S.Q., Sun, D.Z., Wang, S.X., Qu, W.J., Markey, R.J., Stein, H.J., Morgan, J.W., Malinovskiy, D., 2004. Preparation and certification of Re-Os dating reference materials: Molybdenites HLP and JDC. Geostandards and Geoanalytical Research 28, 41-52.
Gao, S., Liu, X., Yuan, H., Hattendorf, B., Günther, D., Chen, L., Hu, S., 2002. Determination of Forty Two Major and Trace Elements in USGS and NIST SRM Glasses by Laser Ablation-Inductively Coupled Plasma-Mass Spectrometry. Geostandards Newsletter 26, 181-196.
Gillis, M.X., 2007. Technical Report for the Zuun Mod Molybdenum-Copper-Rhenium project in Bayankhongor aimar, Mongolia, Ulaanbaatar, Mongolia, p. 77.
Gonchigjav, N., Bat-Erdene, G., Altankhuyag, G., Bayarsaikhan, D., 2010. Report on exploration project licensed as 4476X carried out on the Zuun Mod Mo-Cu deposit between 2002-2008, Shinejinst soum, Bayankhongor province, Ulaanbaatar, Mongolia (in Mongolian).
Griffin, W.L., Powell, W.J., Pearson, N.J., O'Reilly, S.Y., 2008. GLITTER: Data reduction software for laser ablation ICP-MS, In: Sylvester, P. (Ed.), Laser Ablation-ICP-MS in the Earth Sciences: Current practices and outstanding issues. Mineralogical Association of Canada, pp. 308-311.
Hanžl, P., Janoušek, V., Hrdličková, K., Buriánek, D., Gerel, O., Altanbaatar, B., Hora, J.M., Čoupek, P., 2023. From magmatic arc to a post-accretionary setting: Late Palaeozoic granitoid plutons in the northwestern Trans-Altai Zone, Mongolia. Journal of Geosciences 68, 25-66.
Harris, N.B.W., Pearce, J.A., Tindle, A.G., 1986. Geochemical characteristics of collision-zone magmatism. Geological Society, London, Special Publications 19, 67-81.
Hildreth, W., Moorbath, S., 1988. Crustal contributions to arc magmatism in the Andes of Central Chile. Contributions to Mineralogy and Petrology 98, 455-489.
Hoshino, M., Sanematsu, K., Watanabe, Y., 2016. Chapter 279 - REE Mineralogy and Resources, In: Jean-Claude, B., Vitalij K, P. (Eds.), Handbook on the Physics and Chemistry of Rare Earths. Elsevier, pp. 129-291.
Hoskin, P.W.O., Schaltegger, U., 2003. The composition of zircon and igneous and metamorphic petrogenesis. Reviews in Mineralogy and Geochemistry 53, 27-62.
Hou, Z., Cook, N.J., 2009. Metallogenesis of the Tibetan collisional orogen: A review and introduction to the special issue. Ore Geology Reviews 36, 2-24.
Hou, Z., Zhang, H., Pan, X., Yang, Z., 2011. Porphyry Cu (–Mo–Au) deposits related to melting of thickened mafic lower crust: Examples from the eastern Tethyan metallogenic domain. Ore Geology Reviews 39, 21-45.
Irvine, T.N., Baragar, W.R.A., 1971. A Guide to the Chemical Classification of the Common Volcanic Rocks. Canadian Journal of Earth Sciences 8, 523-548.
Jahn, B.-M., Wu, F., Chen, B., 2000. Granitoids of the Central Asian Orogenic Belt and continental growth in the Phanerozoic. Earth and Environmental Science Transactions of the Royal Society of Edinburgh 91, 181-193.

John, D.A., Taylor, R.D., 2016. By-products of porphyry copper and molybdenum deposits. Reviews in Economic Geology 18, 137-164.

Johnson, M.C., Rutherford, M.J., Hess, P.C., 1991. Chassigny petrogenesis: Melt compositions, intensive parameters and water contents of Martian (?) magmas. Geochimica et Cosmochimica Acta 55, 349-366.

Khain, E.V., Bibikova, E.V., Kröner, A., Zhuravlev, D.Z., Sklyarov, E.V., Fedotova, A.A., Kravchenko-Berezhnoy, I.R., 2002. The most ancient ophiolite of the Central Asian fold belt: U–Pb and Pb–Pb zircon ages for the Dunzhugur Complex, Eastern Sayan, Siberia, and geodynamic implications. Earth and Planetary Science Letters 199, 311-325.

Khain, E.V., Bibikova, E.V., Salnikova, E.B., Kröner, A., Gibsher, A.S., Didenko, A.N., Degtyarev, K.E., Fedotova, A.A., 2003. The Palaeo-Asian ocean in the Neoproterozoic and early Palaeozoic: New geochronologic data and palaeotectonic reconstructions. Precambrian Research 122, 329-358.

Khashgerel, B.-E., Rye, R.O., Hedenquist, J.W., Kavalieris, I., 2006. Geology and reconnaissance stable isotope study of the Oyu Tolgoi porphyry Cu-Au system, South Gobi, Mongolia. Economic Geology 101, 503-522.

Kirwin, D., Wilson, C., Turmagnai, D., Wolfe, R., 2005. Exploration history, geology, and mineralisation of the Kharmagtai gold–copper porphyry district, South Gobi region, Mongolia, In: Seltmann, R., Gerel, O., Kirwin, D.J. (Eds.), Geodynamics and metallogeny of Mongolia with a special emphasis on copper and gold deposits. SEG-IAGOD Field Trip, 14-16 Aug, 2005, 8th Biennial SGA Meeting., CERCAMS/NHM London, pp. 175-191.

Klemm, L.M., Pettke, T., Heinrich, C.A., Campos, E., 2007. Hydrothermal Evolution of the El Teniente Deposit, Chile: Porphyry Cu-Mo Ore Deposition from Low-Salinity Magmatic Fluids. Economic Geology 102, 1021-1045.

Koprubasi, N., Aldanmaz, E., 2004. Geochemical Constraints on the Petrogenesis of Cenozoic I-Type Granitoids in Northwest Anatolia, Turkey: Evidence for Magma Generation by Lithospheric Delamination in a Post-Collisional Setting. International Geology Review 46, 705-729.

Kröner, A., Windley, B.F., Badarch, G., Tomurtogoo, O., Hegner, E., Jahn, B.M., Gruschka, S., Khain, E.V., Demoux, A., Wingate, M.T.D., Hatcher, R.D., Jr., Carlson, M.P., McBride, J.H., Catalán, J.R.M., 2007. Accretionary growth and crust formation in the Central Asian Orogenic Belt and comparison with the Arabian-Nubian shield, 4-D Framework of Continental Crust-Integrating Crustal Processes through Time. Geological Society of America Memoir, pp. 181-209.

Kuzmichev, A., Kröner, A., Hegner, E., Dunyi, L., Yusheng, W., 2005. The Shishkhid ophiolite, northern Mongolia: A key to the reconstruction of a Neoproterozoic island-arc system in central Asia. Precambrian Research 138, 125-150.

Kuzmichev, A., Sklyarov, E., Postnikov, A., Bibikova, E., 2007. The Oka Belt (Southern Siberia and Northern Mongolia): A Neoproterozoic analog of the Japanese Shimanto Belt? Island Arc 16, 224-242.

Lamb, M.A., Badarch, G., 1997. Paleozoic sedimentary basins and volcanic-arc systems of Southern Mongolia: New stratigraphic and sedimentologic constraints. International Geology Review 39, 542-576.

Landtwing, M.R., Pettke, T., Halter, W.E., Heinrich, C.A., Redmond, P.B., Einaudi, M.T., Kunze, K., 2005. Copper deposition during quartz dissolution by cooling magmatic–hydrothermal fluids: The Bingham porphyry. Earth and Planetary Science Letters 235, 229-243.

Li, J.-X., Qin, K.-Z., Li, G.-M., Xiao, B., Chen, L., Zhao, J.-X., 2011. Post-collisional ore-bearing adakitic porphyries from Gangdese porphyry copper belt, southern Tibet: Melting of thickened juvenile arc lower crust. Lithos 126, 265-277.

Loucks, R.R., 2014. Distinctive composition of copper-ore-forming arcmagmas. Australian Journal of Earth Sciences 61, 5-16.

Ludington, S., Hammarstrom, J., Piatak, N., 2009. Low-fluorine stockwork molybdenite deposits. US Geological Survey open-file report 1211.

Ludington, S., Plumlee, G.S., 2009. Climax-type porphyry molybdenum deposits. US geological survey open-file report 1215, 2009.

Ludwig, K., 2003. User's manual for IsoPlot 3.0. A geochronological toolkit for Microsoft Excel 71.

Ludwig, K.R., 1980. Calculation of uncertainties of U-Pb isotope data. Earth and Planetary Science Letters 46, 212-220.

Martin, H., Smithies, R.H., Rapp, R., Moyen, J.F., Champion, D., 2005. An overview of adakite, tonalite–trondhjemite–granodiorite (TTG), and sanukitoid: relationships and some implications for crustal evolution. Lithos 79, 1-24.

McDonough, W.F., Sun, S.s., 1995. The composition of the Earth. Chemical Geology 120, 223-253.

Merzbacher, C., Eggler, D.H., 1984. A magmatic geohygrometer: Application to Mount St. Helens and other dacitic magmas. Geology 12, 587-590.

Middlemost, E.A.K., 1994. Naming materials in the magma/igneous rock system. Earth-Science Reviews 37, 215-224.

Milam, K.A., McSween Jr., H.Y., Moersch, J., Christensen, P.R., 2010. Distribution and variation of plagioclase compositions on Mars. Journal of Geophysical Research: Planets 115.

Mossakovsky, A.A., Ruzhentsev, S.V., Samygin, S.G., Kheraskova, T.N., 1993. Central Asian fold belt: geodynamic evolution and history of formation. Geotectonics 6, 3-33.

Müntener, O., Kelemen, P.B., Grove, T.L., 2001. The role of H2O during crystallization of primitive arc magmas under uppermost mantle conditions and genesis of igneous pyroxenites: an experimental study. Contributions to Mineralogy and Petrology 141, 643-658.

Müntener, O., Ulmer, P., 2006. Experimentally derived high-pressure cumulates from hydrous arc magmas and consequences for the seismic velocity structure of lower arc crust. Geophysical Research Letters 33.

Osterman, C., 2003. The Zuun Mod project, Bayankhongor aimag: Results of drilling. Internal report for Gallant Minerals and WMC., Ulaanbaatar, Mongolia, p. 28.

Paces, J.B., Miller Jr., J.D., 1993. Precise U-Pb ages of Duluth Complex and related mafic intrusions, northeastern Minnesota: Geochronological insights to physical, petrogenetic, paleomagnetic, and tectonomagmatic processes associated with the 1.1 Ga Midcontinent Rift System. Journal of Geophysical Research: Solid Earth 98, 13997-14013.

Park, J.-W., Campbell, I.H., Chiaradia, M., Hao, H., Lee, C.-T., 2021. Crustal magmatic controls on the formation of porphyry copper deposits. Nature Reviews Earth & Environment 2, 542-557.

Pearce, J.A., Harris, N., Tindle, A.G., 1984. Trace element discrimination diagrams for the tectonic interpretation of granitic rocks. Journal of Petrology 25, 956-983.

Peccerillo, A., Taylor, S.R., 1976. Geochemistry of eocene calc-alkaline volcanic rocks from the Kastamonu area, Northern Turkey. Contributions to Mineralogy and Petrology 58, 63-81.

Petford, N., Gallagher, K., 2001. Partial melting of mafic (amphibolitic) lower crust by periodic influx of basaltic magma. Earth and Planetary Science Letters 193, 483-499.

Pettke, T., Oberli, F., Heinrich, C.A., 2010. The magma and metal source of giant porphyry-type ore deposits, based on lead isotope microanalysis of individual fluid inclusions. Earth and Planetary Science Letters 296, 267-277.

Redmond, P.B., Einaudi, M.T., Inan, E.E., Landtwing, M.R., Heinrich, C.A., 2004. Copper deposition by fluid cooling in intrusion-centered systems: New insights from the Bingham porphyry ore deposit, Utah. Geology 32, 217-220.

Richards, J.P., 2003. Tectono-magmatic precursors for porphyry Cu-(Mo-Au) deposit formation. Economic Geology 98, 1515-1533.

Richards, J.P., 2009. Postsubduction porphyry Cu-Au and epithermal Au deposits: Products of remelting of subduction-modified lithosphere. Geology 37, 247-250.

Richards, J.P., 2011. High Sr/Y arc magmas and porphyry Cu ± Mo ± Au deposits: Just add water. Economic Geology 106, 1075-1081.

Richards, J.P., 2015. Tectonic, magmatic, and metallogenic evolution of the Tethyan orogen: From subduction to collision. Ore Geology Reviews 70, 323-345.

Richards, J.P., 2018. A shake-up in the porphyry world? Economic Geology 113, 1225-1233.

Richards, J.P., 2021. Porphyry copper deposit formation in arcs: What are the odds? Geosphere 18, 130-155.

Richards, J.P., Kerrich, R., 2007. Special Paper: Adakite-like rocks: Their diverse origins and questionable role in metallogenesis. Economic Geology 102, 537-576.

Richards, J.P., Spell, T., Rameh, E., Razique, A., Fletcher, T., 2012. High Sr/Y Magmas Reflect Arc Maturity, High Magmatic Water Content, and Porphyry Cu ± Mo ± Au Potential: Examples from the Tethyan Arcs of Central and Eastern Iran and Western Pakistan. Economic Geology 107, 295-332.

Ruzhentsev, S., Badarch, G., Voznesenskaya, T., Markova, N., 1990. Evolution of geological processes and metallogeny of Mongolia. Nauka, Moscow.

Seedorff, E., Dilles, J.H., Proffett, J.M., Jr., Einaudi, M.T., Zurcher, L., Stavast, W.J.A., Johnson, D.A., Barton, M.D., Hedenquist, J.W., Thompson, J.F.H., Goldfarb, R.J., Richards, J.P., 2005. Porphyry Deposits: Characteristics and Origin of Hypogene Features, One Hundredth Anniversary Volume. Society of Economic Geologists, p. 0.

Selby, D., Creaser, R.A., 2001. Re-Os geochronology and systematics in molybdenite from the Endako porphyry molybdenum deposit, British Columbia, Canada. Economic Geology 96, 197-204.

Seltmann, R., Porter, T.M., Pirajno, F., 2014. Geodynamics and metallogeny of the central Eurasian porphyry and related epithermal mineral systems: A review. Journal of Asian Earth Sciences 79, 810-841.

Sengör, A.M.C., Natal'in, B.A., 1996. Paleotectonics of Asia: fragments of a synthesis, In: Yin, A., Harrison, M. (Eds.), The Tectonic Evolution of Asia. Cambridge University Press, Cambridge, pp. 486-640.

Sengör, A.M.C., Natal'in, B.A., Burtman, V.S., 1993. Evolution of the Altaid tectonic collage and Palaeozoic crustal growth in Eurasia. Nature 364, 299-307.

Seo, J.H., Guillong, M., Heinrich, C.A., 2012. Separation of Molybdenum and Copper in Porphyry Deposits: The Roles of Sulfur, Redox, and pH in Ore Mineral Deposition at Bingham Canyon. Economic Geology 107, 333-356.

Shirey, S.B., Walker, R.J., 1995. Carius Tube Digestion for Low-Blank Rhenium-Osmium Analysis. Analytical Chemistry 67, 2136-2141.

Sillitoe, R.H., 2010. Porphyry Copper Systems*. Economic Geology 105, 3-41.

Sinclair, W., 2007. Porphyry deposits. Mineral deposits of Canada: A synthesis of major deposit-types, district metallogeny, the evolution of geological provinces, and exploration methods: Geological Association of Canada, Mineral Deposits Division, Special Publication 5, 223-243.

Sisson, T.W., Grove, T.L., 1993. Experimental investigations of the role of H2O in calc-alkaline differentiation and subduction zone magmatism. Contributions to Mineralogy and Petrology 113, 143-166.

Smoliar, M.I., Walker, R.J., Morgan, J.W., 1996. Re-Os ages of group IIA, IIIA, IVA, and IVB iron meteorites. Science 271, 1099-1102.

Soesoo, A., 2000. Fractional crystallization of mantle‐derived melts as a mechanism for some I‐type granite petrogenesis: an example from Lachlan Fold Belt, Australia. Journal of the Geological Society 157, 135-149.

Spencer, E.T., Wilkinson, J.J., Creaser, R.A., Seguel, J., 2015. The Distribution and Timing of Molybdenite Mineralization at the El Teniente Cu-Mo Porphyry Deposit, Chile. Economic Geology 110, 387-421.

Stein, H.J., Markey, R.J., Morgan, J.W., Du, A., Sun, Y., 1997. Highly precise and accurate Re-Os ages for molybdenite from the East Qinling molybdenum belt, Shaanxi Province, China. Economic Geology 92, 827-835.

Stein, H.J., Sundblad, K., Markey, R.J., Morgan, J.W., Motuza, G., 1998. Re-Os ages for Archean molybdenite and pyrite, Kuittila-Kivisuo, Finland and Proterozoic molybdenite, Kabeliai, Lithuania: testing the chronometer in a metamorphic and metasomatic setting. Mineralium Deposita 33, 329-345.

Sun, W., Huang, R., Li, H., Yongbin, h., Zhang, C.-c., Sun, S., Zhang, L., Ding, X., Li, C., Zartman, R., Ling, M.-X., 2015. Porphyry deposits and oxidized magmas. Ore Geology Reviews 65, 97–131.

Tang, L., Chen, P.-L., Santosh, M., Zhang, S.-T., Xu, B., Wan, L.-M., Won Kim, S., Sheng, Y.-M., Hu, X.-K., 2022. Geology and genesis of auriferous porphyritic monzogranite and its correlation with the Qiyugou porphyry-breccia system in East Qinling, Central China. Ore Geology Reviews 142, 104709.

Tang, M., Erdman, M., Eldridge, G., Lee, C.-T.A., 2018. The redox "filter" beneath magmatic orogens and the formation of continental crust. Science Advances 4, eaar4444.

Tatsumi, Y., Hamilton, D.L., Nesbitt, R.W., 1986. Chemical characteristics of fluid phase released from a subducted lithosphere and origin of arc magmas: Evidence from high-pressure experiments and natural rocks. Journal of Volcanology and Geothermal Research 29, 293-309.

Taylor, R.D., Hammarstrom, J.M., Piatak, N.M., Seal II, R.R., 2012. Arc-related porphyry molybdenum deposit model: Chapter D in Mineral deposit models for resource assessment. US Geological Survey.

Togtokh, J., Gunbileg, G., 2013. Metallogeny and geochronology of granitoids of the Edren subterrain. Mongolian Explorer 48, 173-183 (in Mongolian).

Togtokh, J., Tumurchudur, C., Lkhundev, S., Oyunchimeg, T., Ganbayar, G., Khulan, B., 2020. Geochronology and composition of granitoid rocks in the Edren terrane and tectonic implications. Mongolian Explorer 62, 45-63 (in Mongolian).

Tosdal, R.M., Dilles, J.H., 2020. Creation of Permeability in the Porphyry Cu Environment. Reviews in Economic Geology 21, 173-204.

Tosdal, R.M., Richards, J.P., 2001. Magmatic and Structural Controls on the Development of Porphyry Cu ± Mo ± Au Deposits. Reviews in Economic Geology 14, 157-181.

Tumurkhuu, D., Otgonbaatar, D., Enkhtuvshin, R., Enkhjargal, B., Ariunchimeg, Y., Tungalag, N., Budsuren, B., Ganzorig, R., Erdenetsogt, K., 2010. South Mongolian island arcs. Institute of Geology and Mineral resources, Ulaanbaatar, Mongolia (in Mongolian).

Tumurkhuu, D., Tumurtogoo, O., Otgonbaatar, D., Narantsesteg, T., Orolmaa, D., Ariunbileg, S., Badamgarav, J., Eenjin, G., Oyunchimeg, T., Oyunchimeg, T., Tungalag, N., Delgerzaya, P., Enkhjargal, B., Uugantsetseg, B., Dolgorsuren, K., Battushig, A., Enkh-Orshikh, O., Tumurkhuu, Y., Erdenebaatar, B., 2013. Geodynamic amd mineralization in the folded belt of South Mongolia., Ulaanbaatar, Mongolia (in Mongolian).

Tungalag, N., Jargalan, S., Khashgerel, B.-E., Mijiddorj, C., Kavalieris, I., 2019. Characteristics of the Late Devonian Tsagaan Suvarga Cu–Mo deposit, Southern Mongolia. Mineralium Deposita 54, 369-380.

Vigar, A.J., Geostast, G.C., Lally, J.H., 2015. Independent technical report Kharmagtai copper gold project, Mongolia.

Voudouris, P., Melfos, V., Spry, P.G., Bindi, L., Moritz, R., Ortelli, M., Kartal, T., 2013. Extremely Re-Rich Molybdenite from Porphyry Cu-Mo-Au Prospects in Northeastern Greece: Mode of Occurrence, Causes of Enrichment, and Implications for Gold Exploration. Minerals 3, 165-191.

Wainwright, A.J., Tosdal, R.M., Forster, C.N., Kirwin, D.J., Lewis, P.D., Wooden, J.L., 2011a. Devonian and Carboniferous arcs of the Oyu Tolgoi porphyry Cu-Au district, South Gobi region, Mongolia. GSA Bulletin 123, 306-328.

Wainwright, A.J., Tosdal, R.M., Wooden, J.L., Mazdab, F.K., Friedman, R.M., 2011b. U–Pb (zircon) and geochemical constraints on the age, origin, and evolution of Paleozoic arc magmas in the Oyu Tolgoi porphyry Cu–Au district, southern Mongolia. Gondwana Research 19, 764-787.

Watanabe, Y., Stein, H.J., 2000. Re-Os ages for the Erdenet and Tsagaan Suvarga porphyry Cu-Mo deposits, Mongolia, and tectonic implications. Economic Geology 95, 1537-1542.

Westra, G., Keith, S.B., 1981. Classification and genesis of stockwork molybdenum deposits. Economic Geology 76, 844-873.

Windley, B.F., Alexeiev, D., Xiao, W., Kröner, A., Badarch, G., 2007. Tectonic models for accretion of the Central Asian Orogenic Belt. Journal of the Geological Society 164, 31.

Wu, Y.-S., Chen, Y.-J., Zhou, K.-F., 2017. Mo deposits in Northwest China: Geology, geochemistry, geochronology and tectonic setting. Ore Geology Reviews 81, 641-671.

Xiao, W., Windley, B.F., Hao, J., Zhai, M., 2003. Accretion leading to collision and the Permian Solonker suture, Inner Mongolia, China: Termination of the central Asian orogenic belt. Tectonics 22.

Yakubchuk, A., 2002. The Baikalide-Altaid, Transbaikal-Mongolian and North Pacific orogenic collages: similarity and diversity of structural patterns and metallogenic zoning. Geological Society, London, Special Publications 204, 273.

Yakubchuk, A., 2005. Geodynamic evolution of accreted terranes of Mongolia against the backgroun of the Altaids and Transbaikal-Mongolian collages, In: Seltmann, R., Gerel, O., Kirwin, D.J. (Eds.), Geodynamics and metallogeny of Mongolia with a special emphasis on copper and gold deposits. SEG-IAGOD Field Trip, 14-16 Aug, 2005, 8th Biennial SGA Meeting., CERCAMS/NHM London, pp. 13-24.

Yakubchuk, A., Cole, A., Seltmann, R., Shatov, V., 2002. Tectonic Setting, Characteristics, and Regional Exploration Criteria for Gold Mineralization in the Altaid Orogenic Collage: The Tien Shan Province as a Key Example, In: Goldfarb, R.J., Nielsen, R.L. (Eds.), Integrated Methods for Discovery: Global Exploration in the Twenty-First Century. Society of Economic Geologists, pp. 177-201.

Yakubchuk, A., Degtyarev, K., Maslennikov, V., Wurst, A., Stekhin, A., Lobanov, K., 2012. Tectonomagmatic Settings, Architecture, and Metallogeny of the Central Asian Copper Province, In: Hedenquist, J.W., Harris, M., Camus, F. (Eds.), Geology and Genesis of Major Copper Deposits and Districts of the World: A Tribute to Richard H. Sillitoe. Society of Economic Geologists, pp. 403-432.

Yarmolyuk, V., Kovalenko, V., Kovach, V., Rytsk, E.Y., Kozakov, I., Kotov, A., Sal'Nikova, E., 2006. Early stages of the Paleoasian Ocean formation: Results of geochronological, isotopic, and geochemical investigations of Late Riphean and Vendian-Cambrian complexes in the Central Asian Foldbelt, Doklady Earth Sciences. Springer Nature BV, p. 1184.

Yarmolyuk, V.V., Tikhonov, V.I., 1982. Late Paleozoic magmatism and fault tectonics in the Trans-Altai Gobi, Mongolia. Geotectonics 16, 123-130.

Yuan, H., Gao, S., Liu, X., Li, H., Günther, D., Wu, F., 2004. Accurate U-Pb Age and Trace Element Determinations of Zircon by Laser Ablation-Inductively Coupled Plasma-Mass Spectrometry. Geostandards and Geoanalytical Research 28, 353-370.

Zabotkin, L.V., Mosiondz, K.A., Dobrov, G.M., Bochkov, S.V., Nikitin, L.V., Vyertlib, V.I., Klichkov, L.V., Basmanov, V.M., Murashov, V.M., Tsedenbal, C., Eenjin, G., Davaadorj, D., 1988. Report on geological mapping at a scale of 1:200000 in Bayankhongor region, 4276, Ulaanbaatar, Mongolia (in Russian).

Zellmer, G.F., Iizuka, Y., Miyoshi, M., Tamura, Y., Tatsumi, Y., 2012. Lower crustal H2O controls on the formation of adakitic melts. Geology 40, 487-490.

Zeng, Q.-D., Liu, J.-M., Chu, S.-X., Wang, Y.-B., Sun, Y., Duan, X.-X., Zhou, L.-L., Qu, W.-J., 2014. Re–Os and U–Pb geochronology of the Duobaoshan porphyry Cu–Mo–(Au) deposit, northeast China, and its geological significance. Journal of Asian Earth Sciences 79, 895-909.

Zhang, C., Luo, Q., Zhang, X., Liu, L., Liu, D., Wang, P., Yang, K., Wang, J., Zhao, Y., 2018. Geochronological, geochemical, and Sr–Nd–Hf isotopic studies of the Aketas adakitic granites in Eastern Junggar: Petrogenesis and tectonic implications. Geological Journal 53, 80-101.

Fig. 1

Click here to access/download;Figure;Fig. 1.pdf

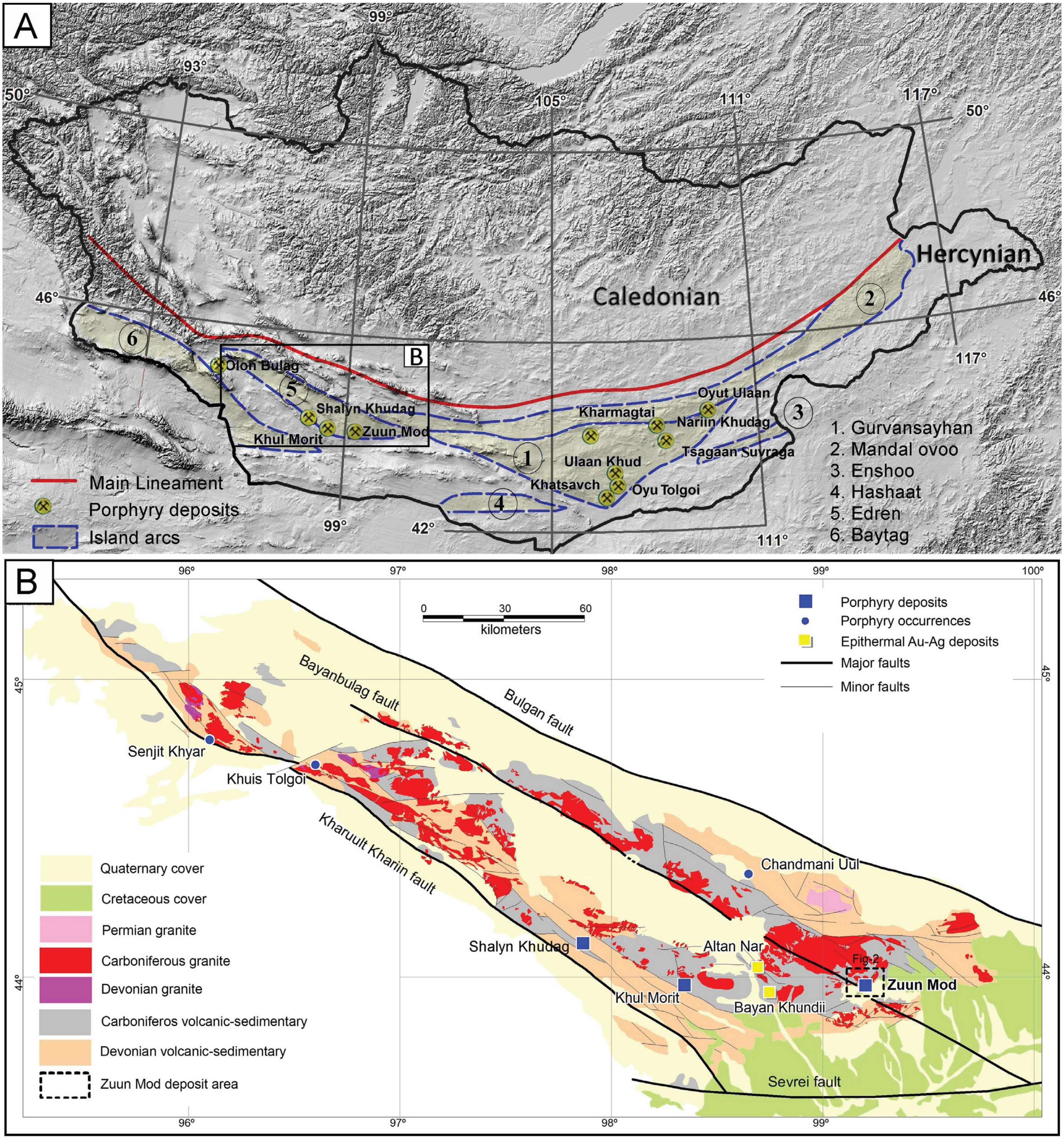

Fig. 2

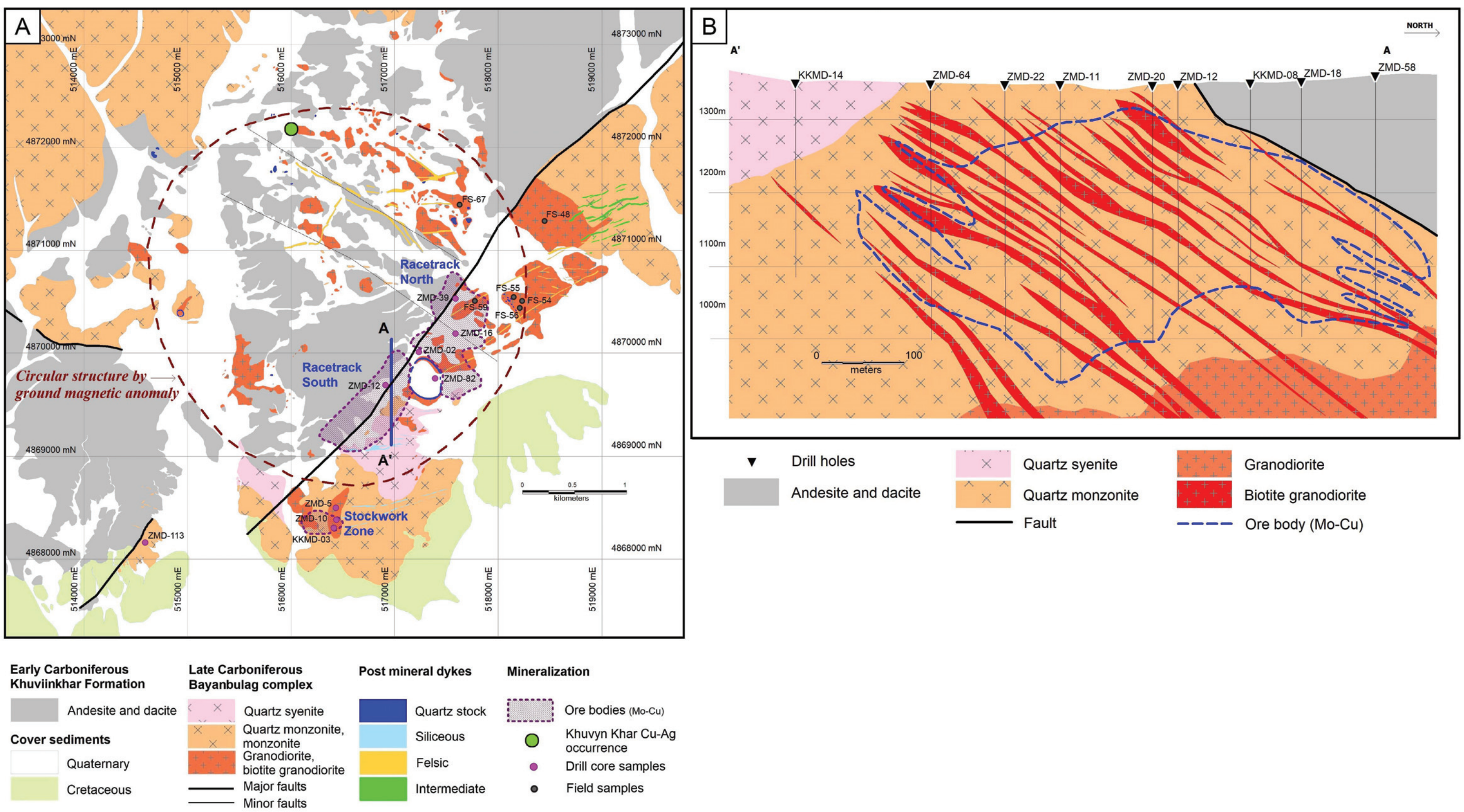
A
B
Circular structure by ground magnetic anomaly
Racetrack North
Racetrack South
Stockwork Zone
A
A'
ZMD-39
ZMD-16
ZMD-02
ZMD-82
ZMD-12
ZMD-5
ZMD-10
KKMD-03
ZMD-113
FS-67
FS-48
FS-55
FS-54
FS-56
4873000 mN
4872000 mN
4871000 mN
4870000 mN
4869000 mN
4868000 mN
514000 mE
515000 mE
516000 mE
517000 mE
518000 mE
519000 mE
kilometers
NORTH
KKMD-14
ZMD-64
ZMD-22
ZMD-11
ZMD-20
ZMD-12
KKMD-08
ZMD-18
ZMD-58
1300m
1200m
1100m
1000m
0
100
meters
Drill holes
Andesite and dacite
Quartz syenite
Quartz monzonite
Fault
Granodiorite
Biotite granodiorite
Ore body (Mo-Cu)
Early Carboniferous Khuviinkhar Formation
Andesite and dacite
Cover sediments
Quaternary
Cretaceous
Late Carboniferous Bayanbulag complex
Quartz syenite
Quartz monzonite, monzonite
Granodiorite, biotite granodiorite
Major faults
Minor faults
Post mineral dykes
Quartz stock
Siliceous
Felsic
Intermediate
Mineralization
Ore bodies (Mo-Cu)
Khuvyn Khar Cu-Ag occurrence
Drill core samples
Field samples

Fig. 3

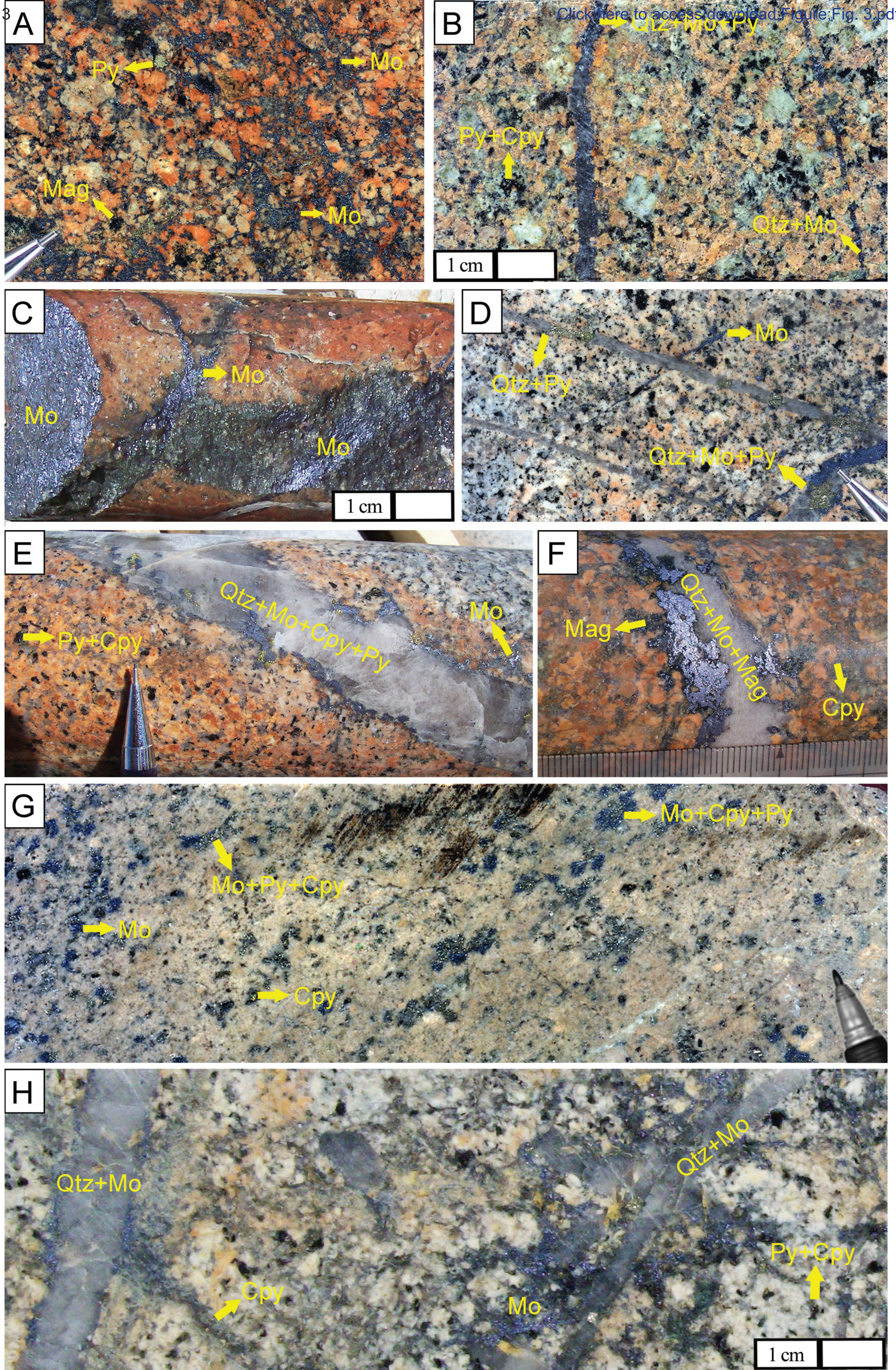
A
Py
Mo
Mag
Mo
B
Qtz+Mo+Py
Py+Cpy
Qtz+Mo
1 cm
C
Mo
Mo
Mo
1 cm
D
Mo
Qtz+Py
Qtz+Mo+Py
E
Qtz+Mo+Cpy+Py
Mo
Py+Cpy
F
Qtz+Mo+Mag
Mag
Cpy
G
Mo+Cpy+Py
Mo+Py+Cpy
Mo
Cpy
H
Qtz+Mo
Qtz+Mo
Cpy
Mo
Py+Cpy
1 cm

Fig. 4

Click here to access/download;Figure;Fig. 4.pdf

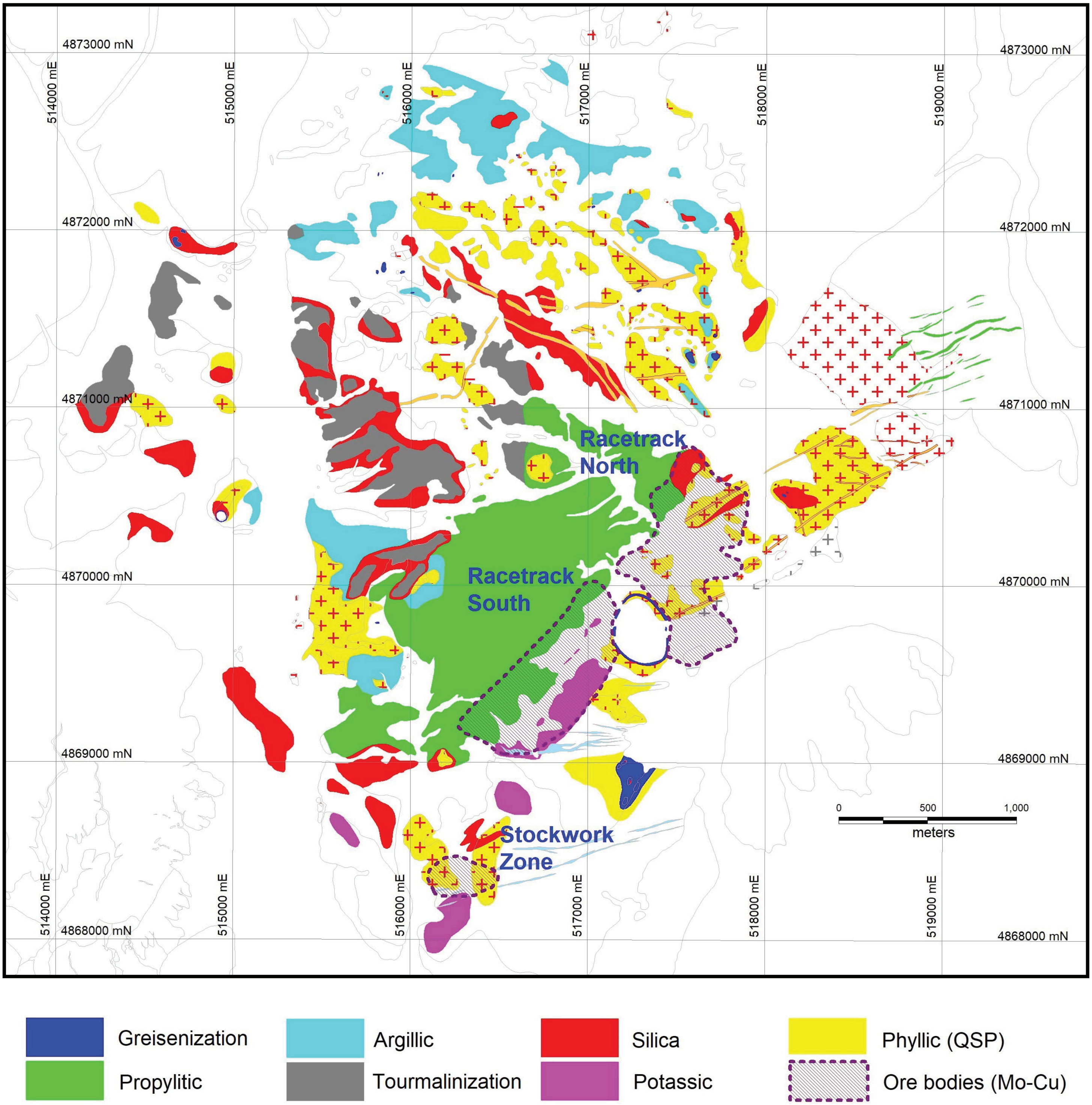

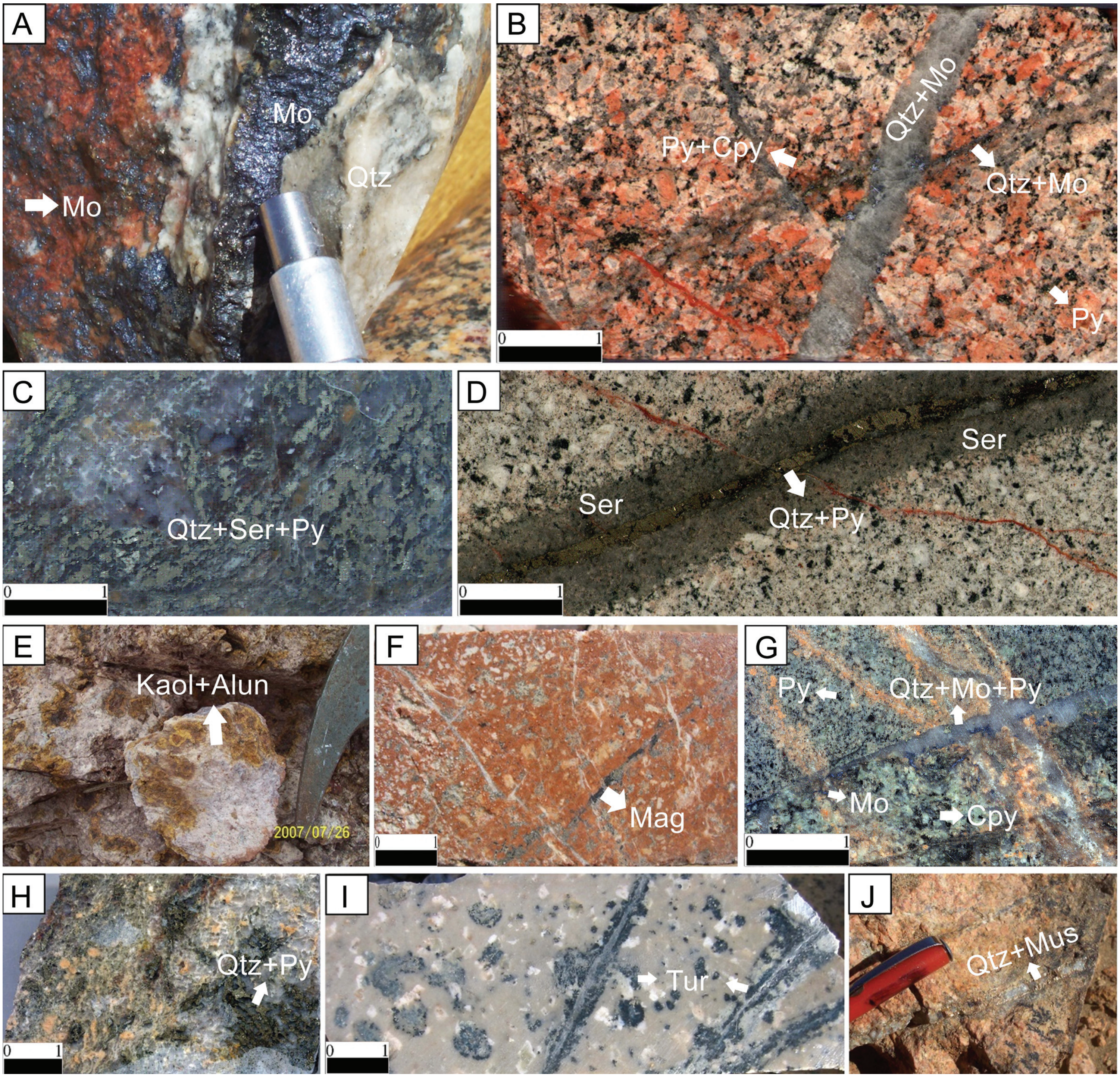
A
Mo
Qtz
Mo
B
Qtz+Mo
Py+Cpy
Qtz+Mo
Py
0
1
C
Qtz+Ser+Py
0
1
D
Ser
Ser
Qtz+Py
0
1
E
Kaol+Alun
2007/07/26
F
Mag
0
1
G
Py
Qtz+Mo+Py
Mo
Cpy
0
1
H
Qtz+Py
0
1
I
Tur
0
1
J
Qtz+Mus

Fig. 6

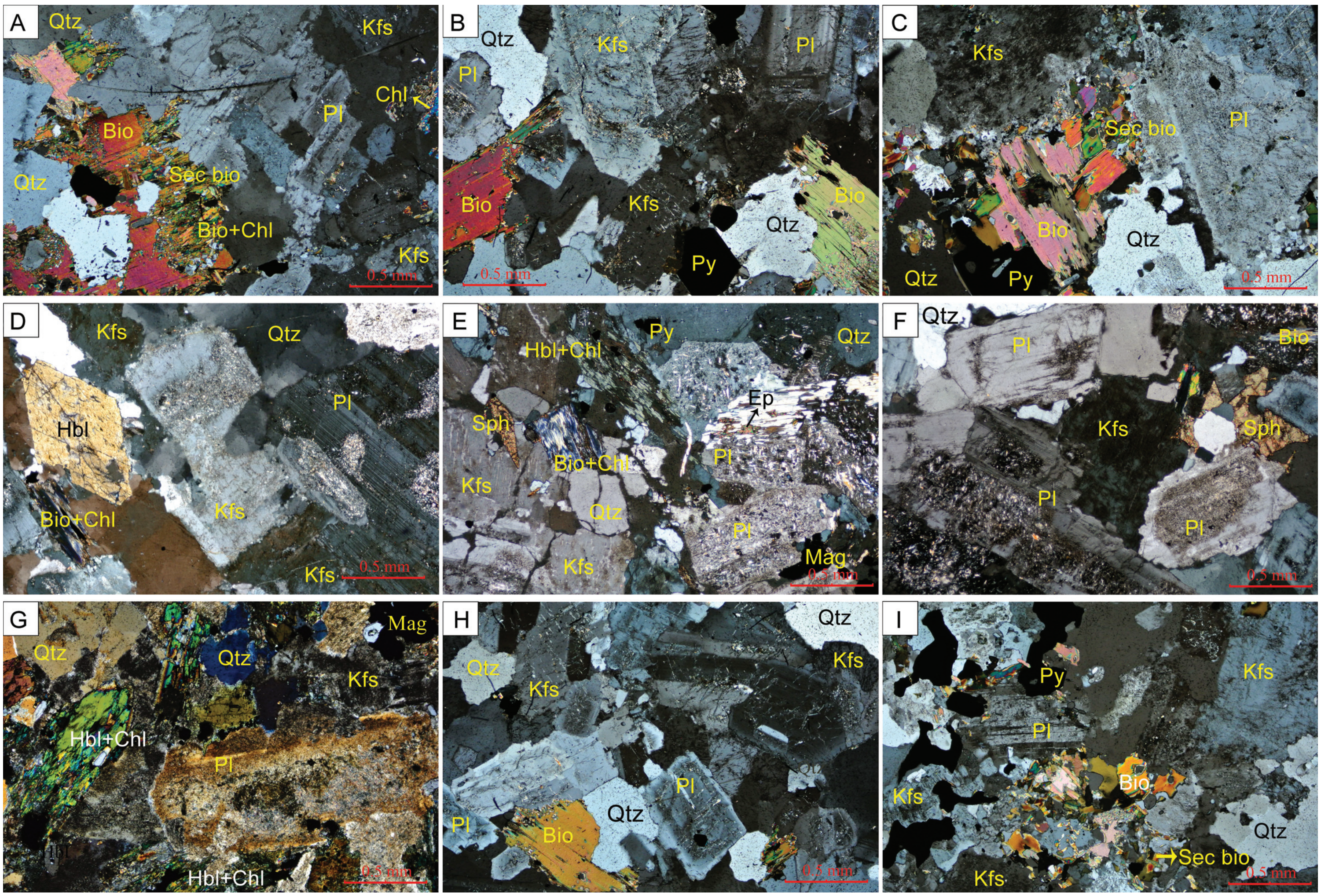
A
Qtz
Kfs
Chl
Pl
Bio
Qtz
Sec bio
Bio+Chl
Kfs
0.5 mm
B
Qtz
Kfs
Pl
Pl
Bio
Kfs
Bio
Qtz
Py
0.5 mm
C
Kfs
Sec bio
Pl
Bio
Qtz
Qtz
Py
0.5 mm
D
Kfs
Qtz
Pl
Hbl
Bio+Chl
Kfs
Kfs
0.5 mm
E
Hbl+Chl
Py
Qtz
Ep
Sph
Bio+Chl
Pl
Kfs
Qtz
Pl
Kfs
Mag
0.5 mm
F
Qtz
Pl
Bio
Kfs
Sph
Pl
Pl
0.5 mm
G
Mag
Qtz
Qtz
Kfs
Hbl+Chl
Pl
Hbl+Chl
0.5 mm
H
Qtz
Kfs
Qtz
Kfs
Pl
Qtz
Pl
Bio
0.5 mm
I
Py
Kfs
Pl
Bio
Kfs
Qtz
Sec bio
Kfs
0.5 mm

Fig. 7

Click here to access/download;Figure;Fig. 7.pdf

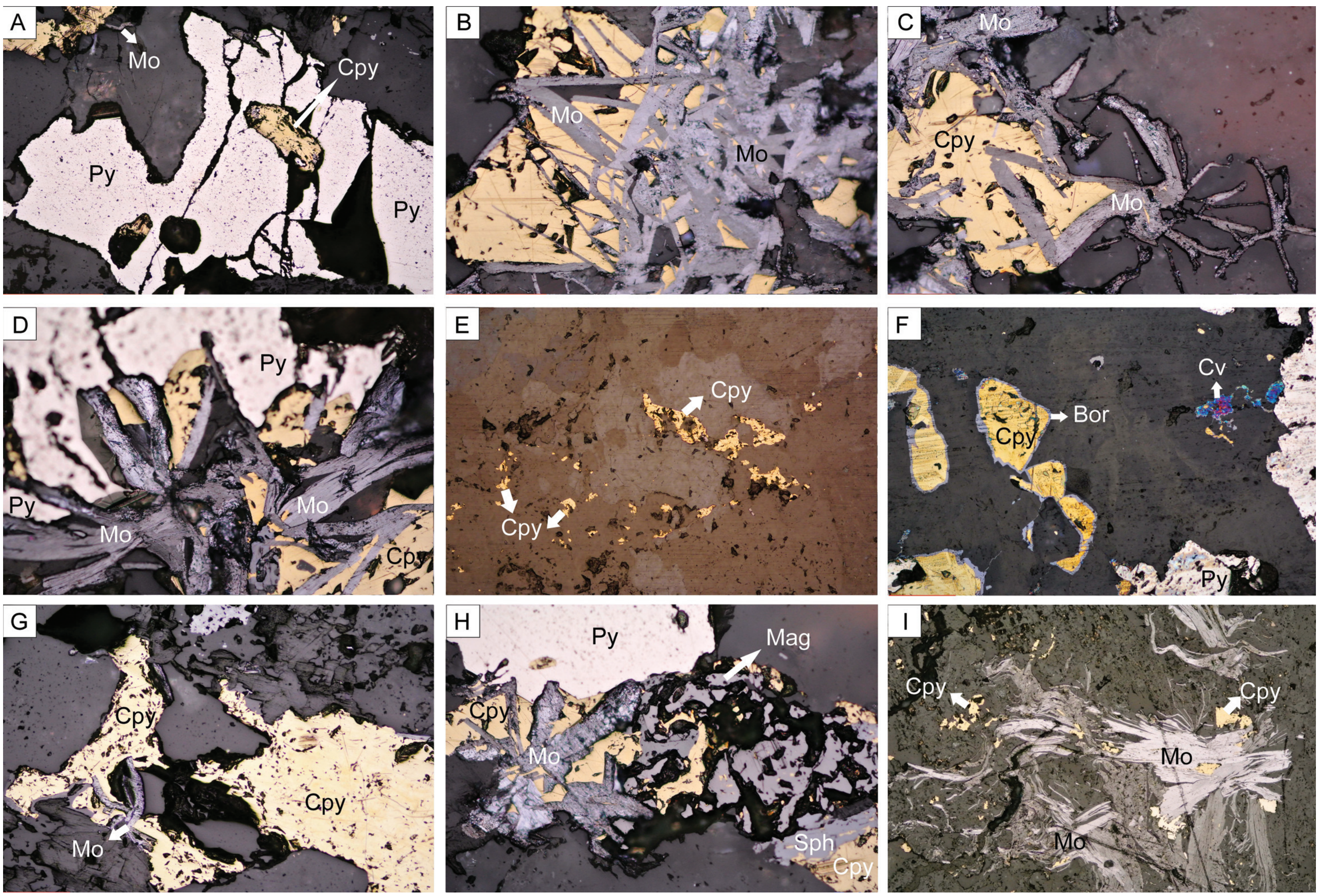

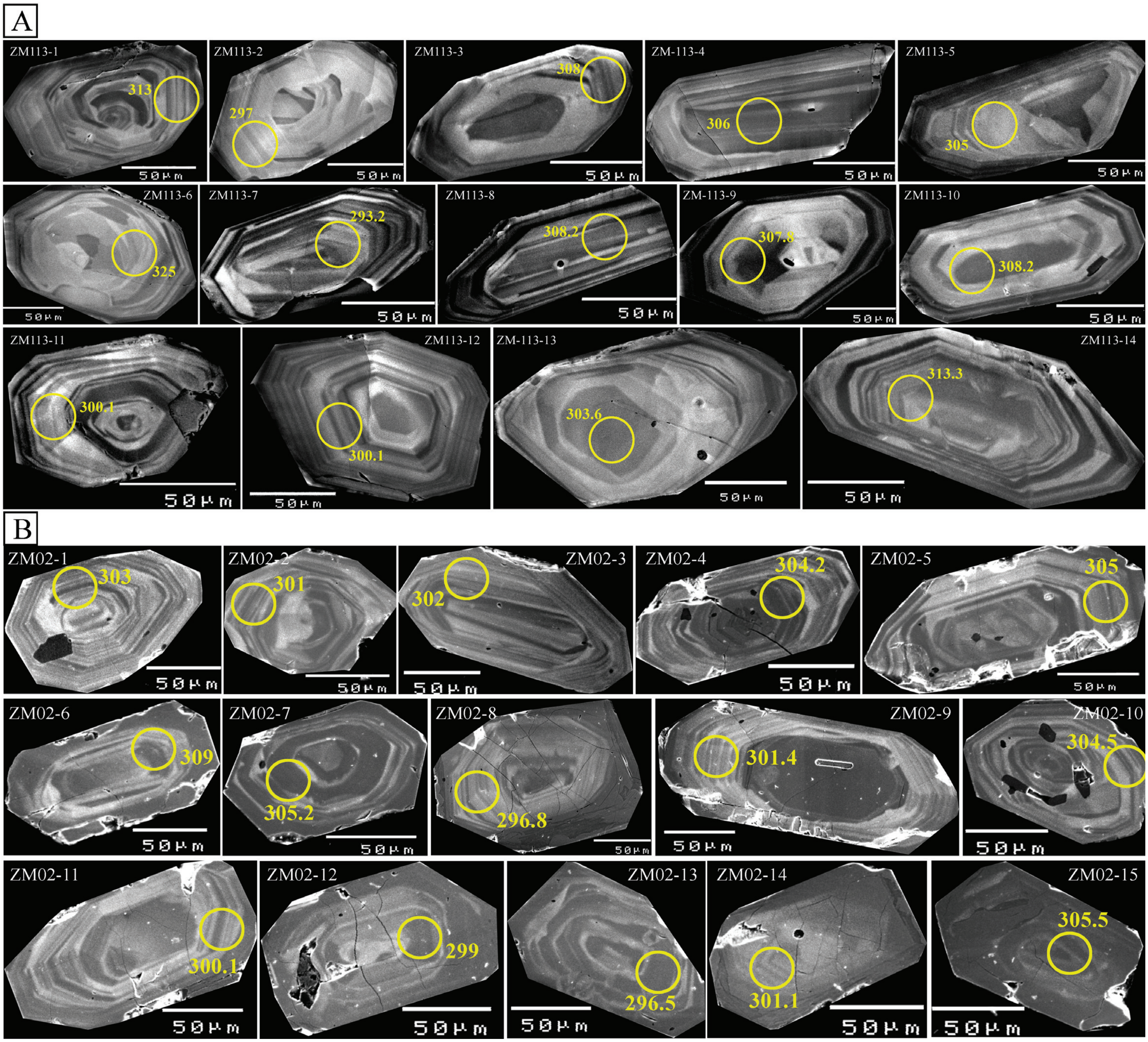
A
ZM113-1
313
ZM113-2
297
ZM113-3
308
ZM-113-4
306
ZM113-5
305
ZM113-6
325
ZM113-7
293.2
ZM113-8
308.2
ZM-113-9
307.8
ZM113-10
308.2
ZM113-11
300.1
ZM113-12
300.1
ZM-113-13
303.6
ZM113-14
313.3
B
ZM02-1
303
ZM02-2
301
ZM02-3
302
ZM02-4
304.2
ZM02-5
305
ZM02-6
309
ZM02-7
305.2
ZM02-8
296.8
ZM02-9
301.4
ZM02-10
304.5
ZM02-11
300.1
ZM02-12
299
ZM02-13
296.5
ZM02-14
301.1
ZM02-15
305.5
50μm

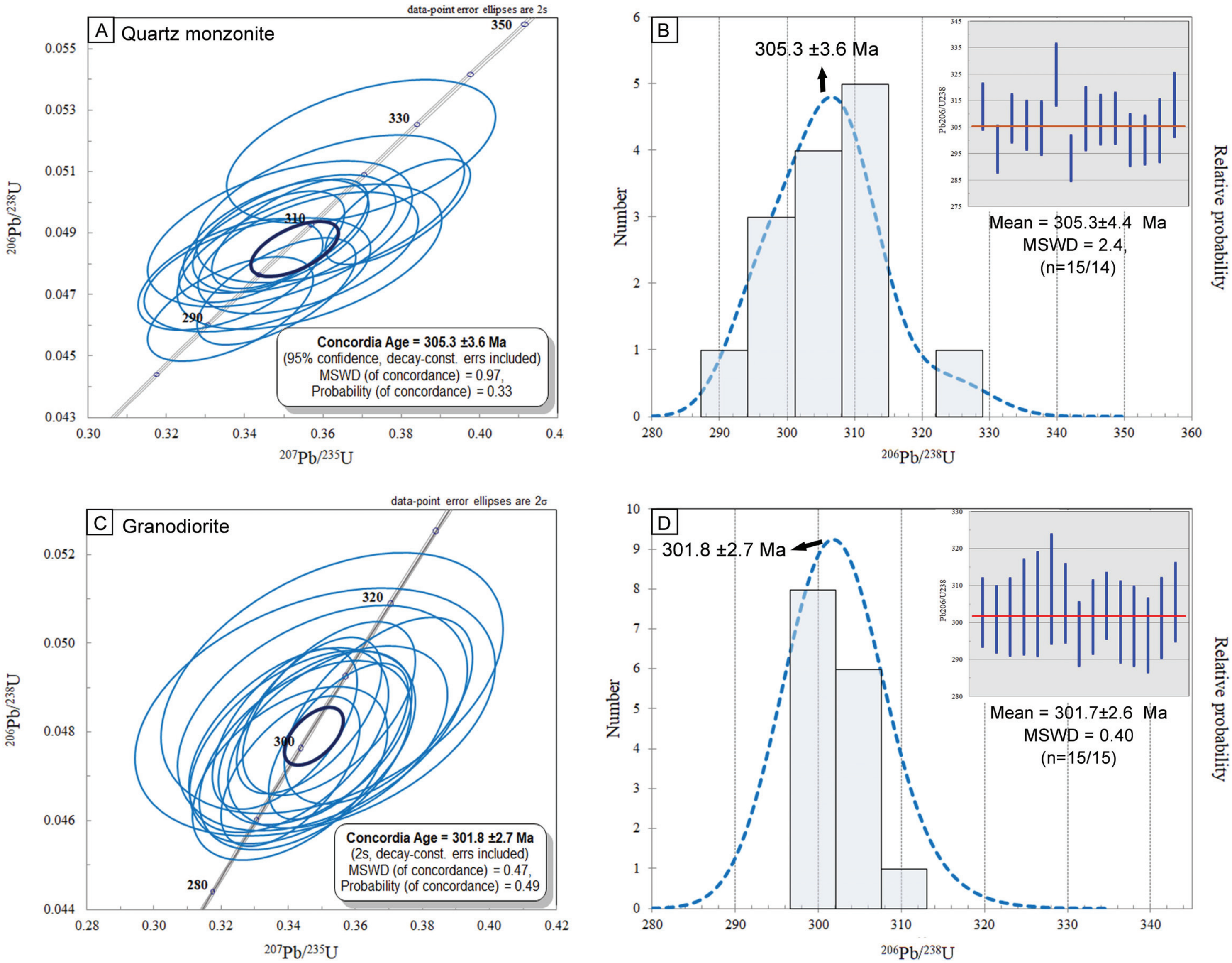
A Quartz monzonite
data-point error ellipses are 2s
Concordia Age = 305.3 ±3.6 Ma
(95% confidence, decay-const. errs included)
MSWD (of concordance) = 0.97,
Probability (of concordance) = 0.33
B
305.3 ±3.6 Ma
Mean = 305.3±4.4 Ma
MSWD = 2.4,
(n=15/14)
Number
Relative probability
C Granodiorite
data-point error ellipses are 2σ
Concordia Age = 301.8 ±2.7 Ma
(2s, decay-const. errs included)
MSWD (of concordance) = 0.47,
Probability (of concordance) = 0.49
D
301.8 ±2.7 Ma
Mean = 301.7±2.6 Ma
MSWD = 0.40
(n=15/15)
$^{206}Pb/^{238}U$
$^{207}Pb/^{235}U$

Fig. 10

Click here to access/download;Figure;Fig. 10.pdf

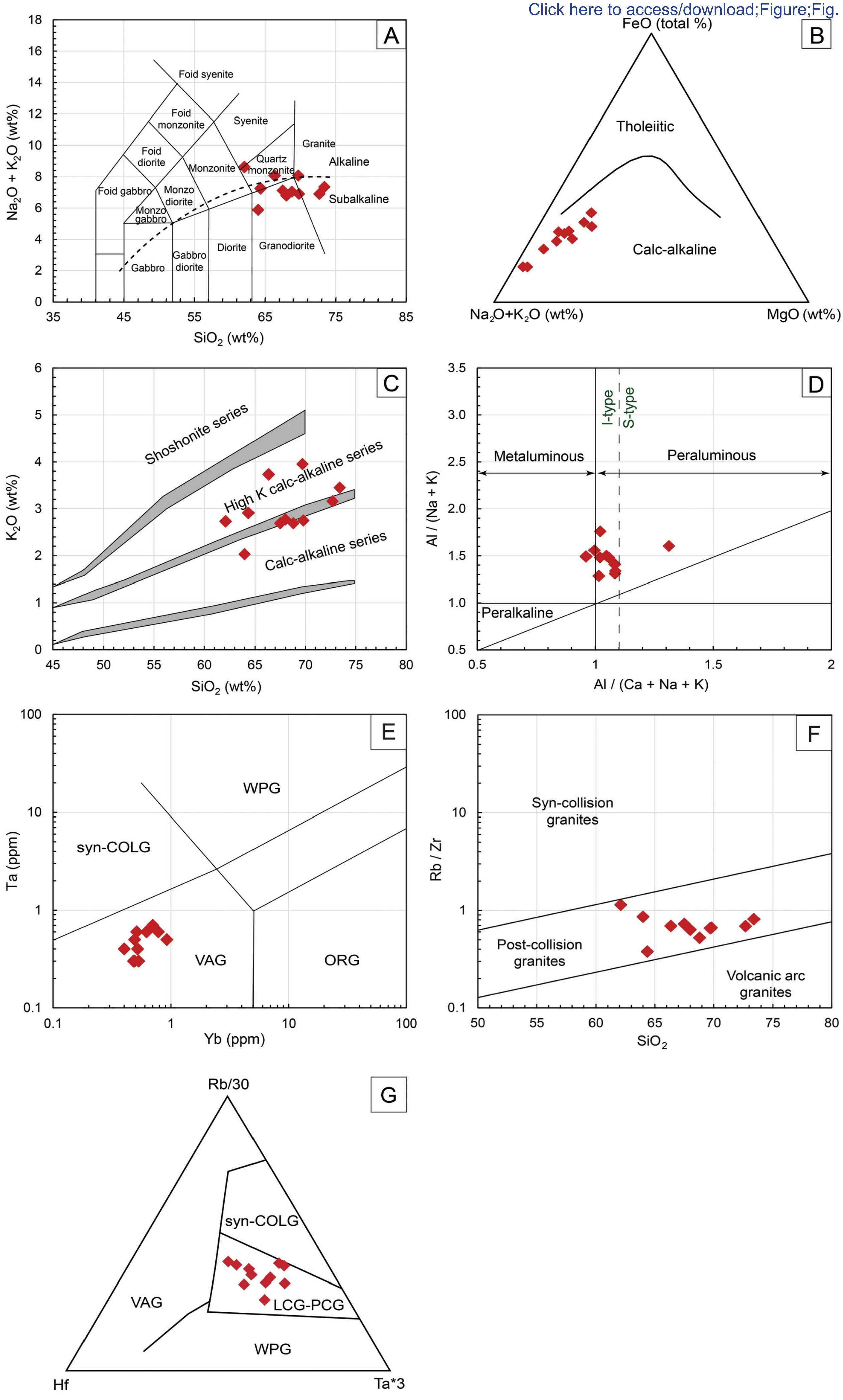

Fig. 11 Click here to access/download;Figure;Fig. 11.pdf

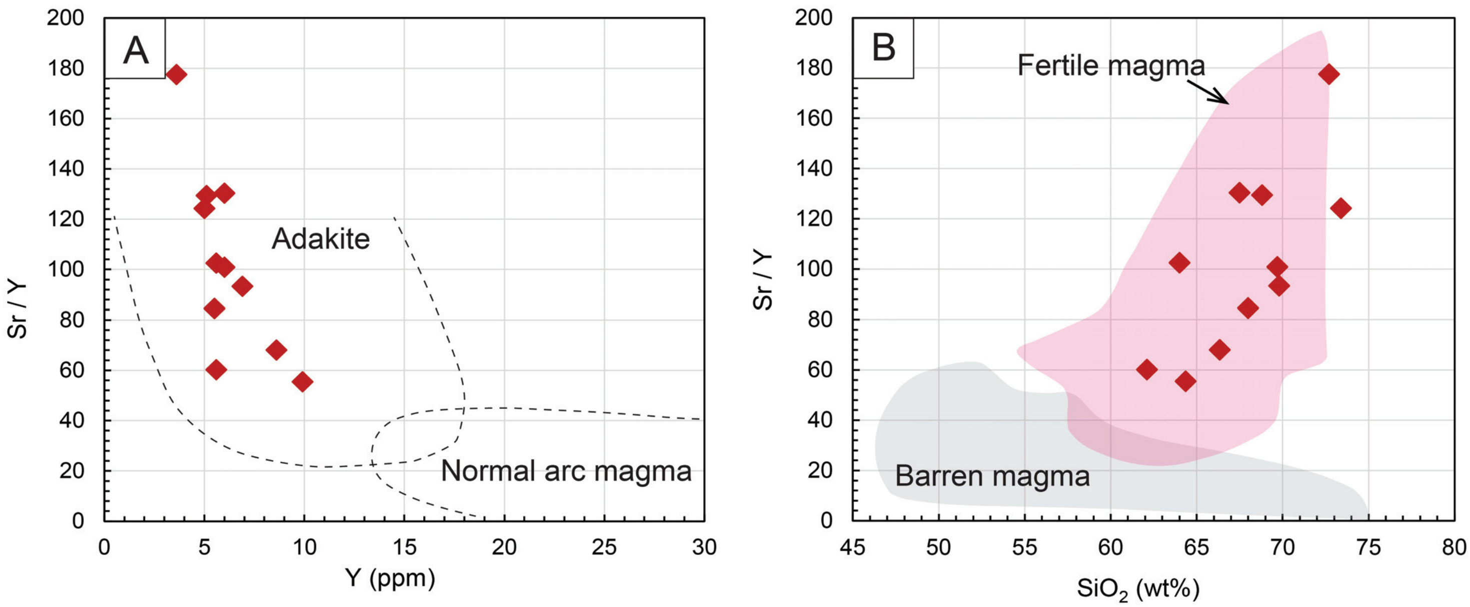

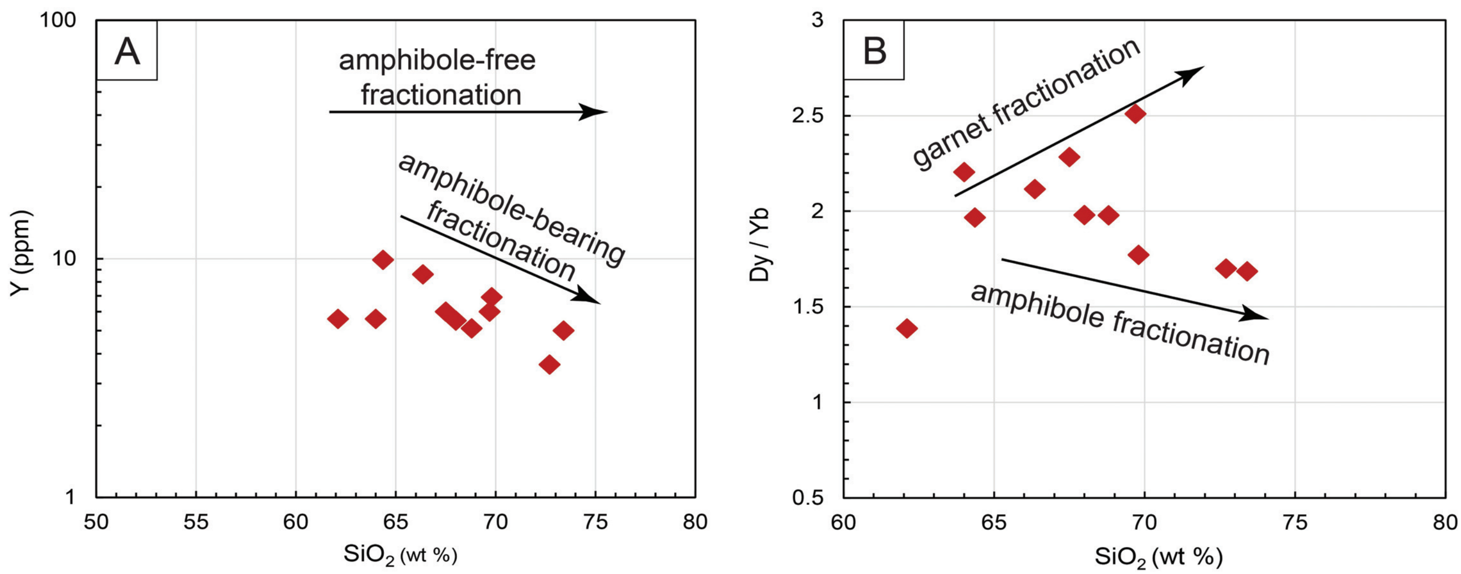
A
amphibole-free
fractionation
amphibole-bearing
fractionation
Y (ppm)
100
10
1
50
55
60
65
70
75
80
SiO2 (wt %)
B
garnet fractionation
amphibole fractionation
Dy / Yb
3
2.5
2
1.5
1
0.5
60
65
70
75
80
SiO2 (wt %)

Fig. 13 Click here to access/download;Figure;Fig. 13.pdf

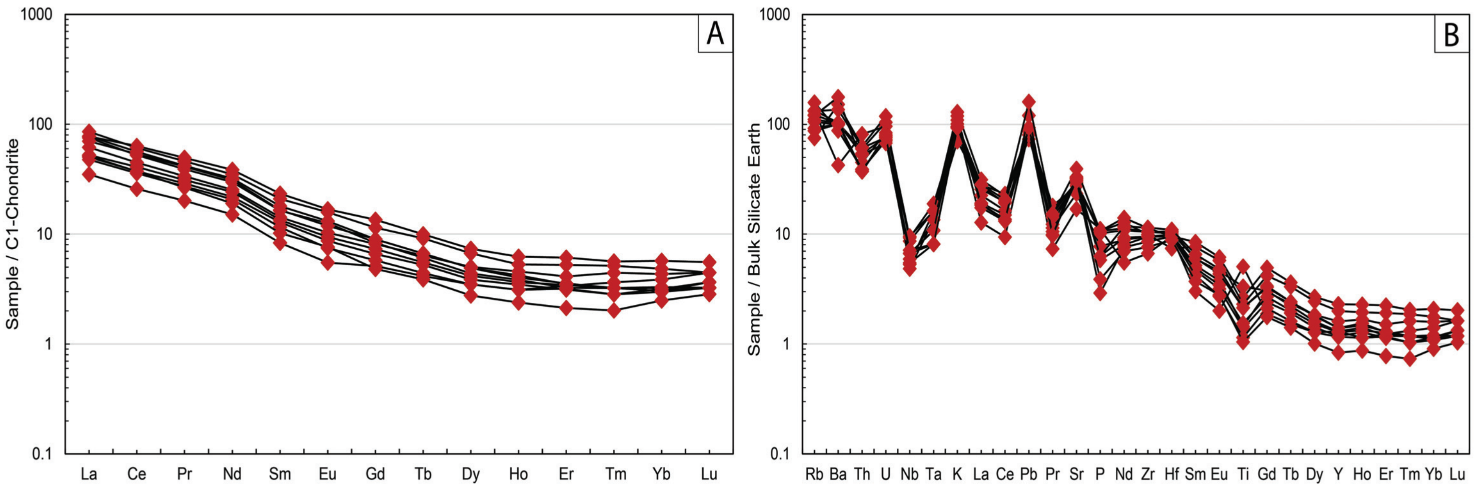

Fig. 14

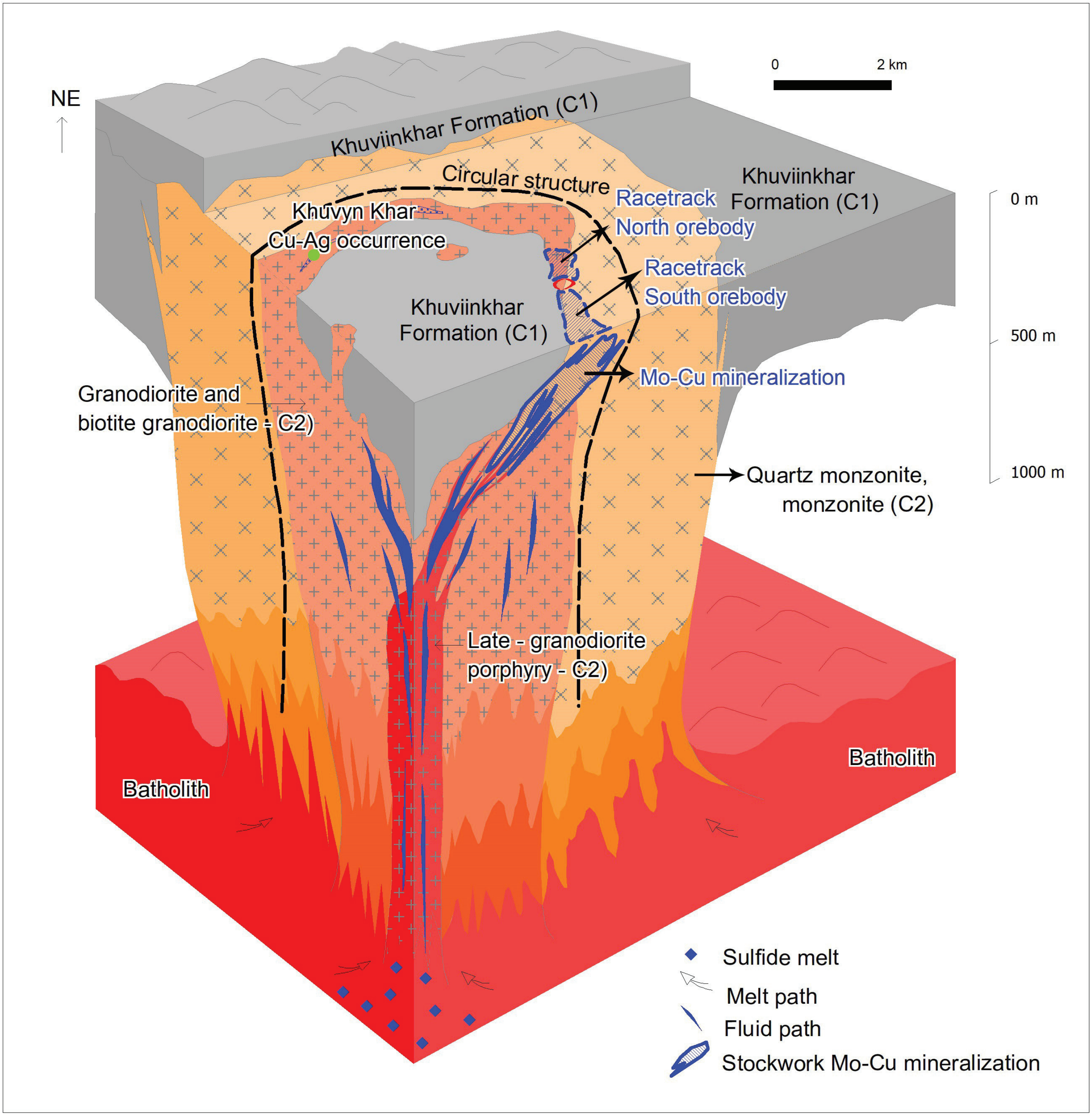

NE
0
2 km
Khuviinkhar Formation (C1)
Circular structure
Khuvyn Khar
Cu-Ag occurrence
Racetrack
North orebody
Khuviinkhar
Formation (C1)
0 m
Racetrack
South orebody
Khuviinkhar
Formation (C1)
500 m
Mo-Cu mineralization
Granodiorite and
biotite granodiorite - C2)
1000 m
Quartz monzonite,
monzonite (C2)
Late - granodiorite
porphyry - C2)
Batholith
Batholith
Sulfide melt
Melt path
Fluid path
Stockwork Mo-Cu mineralization

Table 1. Isotopic data of U-Pb age determinations on zircon grains collected from the Bayanbulag intrusive complex

No	Spots	Measured isotopic ratios						204 corrected (if RSD < 10%) age (Ma)				Th/U	Dis (%)	For Concordia diagram using Isoplot				
		$^{204}Pb/^{206}Pb$	$^{232}Th/^{238}U$	$^{45}Sc/^{89}Y$	$^{207}Pb/^{206}Pb$	$^{206}Pb/^{238}U$	$^{207}Pb/^{235}U$	$^{206}Pb/^{238}U$	±2s	$^{207}Pb/^{235}U$	±2s			$^{207}Pb/^{235}U$	±2s (%)	$^{206}Pb/^{238}U$	±2s (%)	error corrected
1	ZM113-1	0.004	0.434	0.533	0.055	0.05	0.379	312.6	8.62	326.5	11.16	0.434	4.4	0.379	3.997	0.05	2.817	0.705
2	ZM11`3-2	0.003	0.705	0.154	0.054	0.047	0.348	296.6	8.74	303.3	12.44	0.705	2.2	0.348	4.745	0.047	3.015	0.635
3	ZM113-3	0.003	0.645	0.254	0.052	0.049	0.352	308.2	8.98	305.9	12.28	0.645	-0.8	0.352	4.648	0.049	2.981	0.641
4	ZM113-4	0	0.846	0.15	0.051	0.049	0.344	305.6	9.14	300.5	13.02	0.846	-1.7	0.344	5	0.049	3.048	0.61
5	ZM113-5	0.009	0.591	0.417	0.053	0.048	0.356	304.5	9.94	309.4	17.22	0.591	1.6	0.356	6.455	0.048	3.349	0.519
6	ZM113-6	0.001	0.495	0.764	0.052	0.052	0.37	324.7	11.62	319.4	20.84	0.495	-1.6	0.37	7.601	0.052	3.678	0.484
7	ZM113-7	0.005	0.697	0.204	0.052	0.047	0.336	293.1	8.52	294.4	13.12	0.697	0.4	0.336	5.132	0.047	2.966	0.578
8	ZM113-8	-0.006	0.249	0.136	0.052	0.049	0.35	308.1	11.86	304	20.76	0.249	-1.4	0.349	7.891	0.049	3.962	0.502
9	ZM113-9	-0.006	0.876	0.28	0.052	0.049	0.348	307.7	9.16	303.2	14.56	0.876	-1.5	0.348	5.552	0.049	3.067	0.553
10	ZM113-10	-0.004	0.663	0.27	0.052	0.049	0.353	308.2	9.56	306.8	15.94	0.663	-0.5	0.353	6.017	0.049	3.185	0.529
11	ZM113-11	0	0.459	0.568	0.051	0.048	0.336	300	9.66	294.4	15.7	0.459	-1.9	0.336	5.715	0.048	3.106	0.543
12	ZM113-12	0.003	0.486	0.483	0.052	0.048	0.343	300	9.14	299.6	14.52	0.486	-0.2	0.343	6.893	0.048	3.19	0.463
13	ZM113-13	-0.004	1.42	0.151	0.054	0.048	0.357	303.6	11.76	309.7	20.68	1.42	2	0.357	7.739	0.048	3.981	0.514
14	ZM113-14	-0.01	0.79	0.179	0.053	0.05	0.363	313.2	12	313.6	20.9	0.79	0.1	0.362	7.73	0.05	3.936	0.509
15	ZM02-1	-0.006	0.571	0.201	0.051	0.048	0.339	302.6	9.14	296.4	13.42	0.571	-2.1	0.339	5.215	0.048	3.079	0.59
16	ZM02-2	-0.001	0.674	0.194	0.054	0.048	0.355	300.8	8.9	308.4	12.74	0.674	2.5	0.355	4.789	0.048	3.014	0.629
17	ZM02-3	0.003	0.831	0.277	0.054	0.048	0.355	301.4	10.36	308.3	20	0.831	2.2	0.355	7.525	0.048	3.509	0.466
18	ZM02-4	0.002	0.434	0.789	0.053	0.048	0.35	304.1	12.78	304.8	26.48	0.434	0.2	0.35	10.067	0.048	4.306	0.428
19	ZM02-5	-0.002	0.887	0.188	0.052	0.048	0.349	304.9	13.98	303.2	33.06	0.887	-0.6	0.348	12.594	0.048	4.706	0.374
20	ZM02-6	0	0.471	0.629	0.052	0.049	0.354	309	14.72	307	31.32	0.471	-0.7	0.353	11.799	0.049	4.887	0.414
21	ZM02-7	-0.002	0.669	0.307	0.055	0.048	0.367	305.1	10.54	317.3	17.06	0.669	4	0.367	6.253	0.048	3.548	0.567
22	ZM02-8	-0.004	0.787	0.211	0.052	0.047	0.341	296.81	8.52	297.7	12.76	0.787	0.3	0.341	4.95	0.047	2.929	0.592
23	ZM02-9	-0.017	0.622	0.685	0.053	0.048	0.348	301.4	9.86	303.2	17.68	0.622	0.6	0.348	6.744	0.048	3.342	0.496
24	ZM02-10	-0.007	0.461	0.681	0.052	0.048	0.346	304.5	8.82	301.8	13.28	0.461	-0.9	0.346	5.09	0.048	2.977	0.585
25	ZM02-11	-0.007	0.372	0.55	0.052	0.048	0.344	300.1	10.9	300.4	20.76	0.372	0.1	0.344	7.979	0.048	3.735	0.468
26	ZM02-12	0	0.612	0.368	0.053	0.047	0.345	298.9	10.68	301	19.52	0.612	0.7	0.345	7.49	0.047	3.665	0.489
27	ZM02-13	-0.002	0.528	0.382	0.052	0.047	0.341	296.5	9.9	297.6	17.98	0.528	0.4	0.341	6.969	0.047	3.399	0.488
28	ZM02-14	-0.003	0.582	0.79	0.052	0.048	0.34	301.1	10.78	297.3	18.96	0.582	-1.3	0.34	7.124	0.048	3.555	0.499
29	ZM02-15	-0.004	0.498	0.614	0.053	0.049	0.352	305.49	10.56	306.4	18.94	0.498	0.3	0.352	5.964	0.049	3.297	0.553

Table 2 Click here to access/download;Table (Editable version);Table-2.docx

Table 2. Re-Os isotope data for molybdenite sample from the Zuun Mod porphyry Mo-Cu-Re deposit.

Sample ID	Sample weight（g)	Re (ng/g)		Common Os (ng/g)		Re187 (ng/g)		Os187 (ng/g)		Model age (Ma)	
		Measured value	Uncertainty	Measured value	Uncertainty	Measured value	Uncertainty	Measured value	Uncertainty	Measured value	Uncertainty
ZMD-10	0.01091	155325.4	1655.2	<0.0002	-	97631.3	1040.4	481.9	3.2	295.6	4.8
ZMD-10	0.01058	160286.8	1387.6	<0.0002	-	100749.9	872.2	502.1	4.8	298.4	4.9

Table 3. Whole-rock geochemical data for the host granitoids of the Zuun Mod porphyry Mo-Cu deposit in Southwest Mongolia.

No	1	2	3	4	5	6	7	8	9	10	11
Sample ID	ZMD113	ZMD12 202.5	ZMD16 184.5	FS-48	FS-56	FS-67	ZMD02	ZMD82 177.5	FS-54	FS-55	FS-59
SiO_2 (wt %)	62.1	64.36	66.35	69.8	68.8	68	64	67.5	73.4	72.7	69.7
TiO_2	1.02	0.532	0.463	0.29	0.28	0.31	0.67	0.43	0.23	0.21	0.25
Al_2O_3	16.21	15.34	15.72	15.25	14.9	15.4	15	15.3	13.55	14.15	14.45
Fe_2O_3	5.04	4.15	3.35	2.54	3.1	2.98	4.15	3.34	1.28	1.22	2.39
MnO	0.91	0.052	0.055	0.05	0.05	0.06	0.07	0.05	0.01	0.01	0.07
MgO	2.1	2.24	1.67	0.86	0.79	1.01	1.6	1.2	0.23	0.34	0.64
CaO	1.84	3.12	1.84	3.03	2.5	1.17	3.39	2.43	1.3	2.09	1.26
Na_2O	5.88	4.34	4.34	4.15	4.35	4.02	3.85	4.43	3.89	3.74	4.12
K_2O	2.73	2.91	3.73	2.75	2.69	2.77	2.03	2.69	3.45	3.16	3.95
P_2O_5	0.23	0.22	0.22	0.13	0.12	0.16	0.21	0.22	0.06	0.08	0.13
LOI (wt %)	1.21	0.89	1.2	1.1	0.6	3.13	1.59	2.19	1.55	1.39	1.75
V (ppm)	19	110	91	43	43	48	53	68	30	29	35
Cr	10	50	40	10	10	10	10	10	10	10	10
Co	2	9	9	5.1	5.1	6.4	5.8	6.5	0.8	0.7	4.5
Ni	5	30	20	6	7	7	8	7	5	5	6
Cu	44	1340	1330	51	21	40	70	197	46	31	11
Zn	20	40	50	39	46	39	29	30	13	13	68
Rb	79.7	45	72	66.5	52.3	63.3	94.6	80	73.2	55.1	78.9
Sr	337	549	585	644	660	465	574	782	621	639	605
Y	5.6	9.9	8.6	6.9	5.1	5.5	5.6	6	5	3.6	6
Zr	70	119	104	100	100	100	110	110	90	80	120
Nb	5.7	3.2	3.5	6.1	3.6	4.4	3.9	4.4	6.3	4.4	4.7
Ta	0.6	0.5	0.6	0.7	0.3	0.4	0.5	0.3	0.6	0.4	0.3
Ba	280	1000	1169	674	662	652	580	681	673	665	898
Hf	2.7	2.7	2.1	2.8	2.7	2.7	2.9	3	2.7	2.5	3.1
Cs	1.99	9	8	1.41	2.36	1.56	22.6	2.91	2.74	2.86	3.37
Ga	18.2	17	18	17.5	17.9	18.3	19.3	19.8	15.7	17.8	18.3
La	8.3	18.3	20.3	14.6	11.9	12.4	17.8	16.6	11.3	12.2	18.4
Ce	15.8	38.8	37.4	27.4	22.9	25.1	32.2	32.9	22	22.8	34.5
Pr	1.87	4.59	4.27	3.12	2.68	2.89	3.63	3.82	2.52	2.47	3.89
Nd	6.9	17.6	16	11.6	10	11.1	13.6	14.2	9.5	8.7	14.7
Sm	1.23	3.45	3.1	2.11	1.9	1.99	2.42	2.46	1.71	1.51	2.66
Eu	0.31	0.947	0.889	0.58	0.49	0.53	0.71	0.67	0.42	0.43	0.74
Gd	1.02	2.69	2.28	1.62	1.31	1.46	1.66	1.79	1.15	0.96	1.83
Tb	0.15	0.36	0.33	0.23	0.19	0.2	0.22	0.24	0.16	0.14	0.24
Dy	0.86	1.81	1.65	1.24	0.95	1.03	1.08	1.21	0.86	0.68	1.23
Ho	0.17	0.34	0.29	0.25	0.19	0.2	0.21	0.22	0.17	0.13	0.23
Er	0.54	0.98	0.84	0.66	0.5	0.55	0.52	0.57	0.51	0.34	0.56
Tm	0.09	0.139	0.127	0.11	0.07	0.08	0.08	0.08	0.07	0.05	0.08
Yb	0.62	0.92	0.78	0.7	0.48	0.52	0.49	0.53	0.51	0.4	0.49
Lu	0.11	0.137	0.11	0.11	0.08	0.08	0.09	0.08	0.09	0.07	0.08
U	1.95	2.41	1.7	2.11	1.6	1.63	1.44	1.48	1.37	1.55	1.54
Th	6.46	5.03	3.57	4.74	2.96	2.97	3.1	3.05	4.2	4.31	4.86
Pb	13	13	11	12	12	13	14	13	18	14	24
Mo	2	242	151	201	154	197	177	212	181	127	2
W	9	1.3	2.2	1	1	2	6	7	6	3	1
Sn (ppm)	1	1	1	1	1	1	3	1	1	1	1

Appendix 1. Samples included in this study with drillhole ID, depth, lithology, orebody, and analyses carried out

№	Sample ID	Drillhole	Depth, m	Lithology	Location
	U-Pb geochronology (China)				
1	ZM113	ZMD-113	150	Quartz monzonite	Out of ore zone
2	ZM02	ZMD-29	182.1	Granodiorite, 99° 13' 49.7", 43° 59' 40.0"	North zone
	Re-Os Mo geochronology (China)				
1	ZMD-10	ZMD-10	352	Molybdenite in quartz vein within quartz monzonite	Stockwork zone
	Rock petrography				
1	ZMD16 (182)	ZMD-16	182	Granodiorite	North zone
2	ZM02	ZMD-29	182.1	Granodiorite, 99° 13' 49.7", 43° 59' 40.0"	North zone
3	ZMD39 (112)	ZMD-39	112	Granodiorite	North zone
4	ZMD12 (204.5)	ZMD-12	204.5	Quartz monzonite with quartz vein and mafic enclave	South zone
5	ZMD05 (350.5-350.6)	ZMD-05	350.5-350.6	Biotite granite	Stockwork zone
6	KKMD03 (299.4)	KKMD03	299.4	Quartz monzonite cut by quartz vein	Stockwork zone
7	ZM113	ZMD-113	150	Quartz monzonite	Out of ore zone
8	FS-48	Field sample		Granodiorite	Out of ore zone
9	FS-56	Field sample		Granodiorite	Out of ore zone
10	FS-55	Field sample		Biotite granite	Out of ore zone
	Ore mineralogy				
1	ZMD16 (182)	ZMD-16	182	Granodiorite	North zone
2	ZM02	ZMD-29	182.1	Granodiorite, 99° 13' 49.7", 43° 59' 40.0"	North zone
3	ZMD16 (184.5)	ZMD-16	184.5	Granodiorite	North zone
4	ZMD12 (204.5)	ZMD-12	204.5	Quartz monzonite with quartz vein and mafic enclave	South zone
5	ZMD12 (202.5)	ZMD-12	202.5	Biotite granite	South zone
6	ZMD12 (212.5)	ZMD-12	212.5	Potassic altered quartz monzonite	South zone
7	KKMD03 (299.4)	KKMD-03	299.4	Quartz vein in quartz monzonite	Stockwork zone
8	ZMD10	ZMD-10	352	Vein hosted molybdenite in quartz monzonite	Stockwork zone
9	ZM113	ZMD-113	150	Quartz monzonite	Out of ore zone
	Major and Trace elements & XRF (Akita Universiry and Mongolia)				
1	FS-48	Field sample		Granodiorite	Out of ore zone
2	FS-54	Field sample		Leucogranite	Out of ore zone
3	FS-55	Field sample		Leucogranite	Out of ore zone
4	FS-56	Field sample		Granodiorite	Out of ore zone
5	FS-59	Field sample		Biotite granite	Out of ore zone
6	FS-67	Field sample		Granodiorite	Out of ore zone
7	ZM113	ZMD-113	150	Quartz monzonite	Out of ore zone
8	ZMD82 177.5m	ZMD82	177.5	Granodiorite	North zone
9	ZM02	ZMD-29	182.1	Granodiorite, 99° 13' 49.7", 43° 59' 40.0"	North zone
10	ZMD16 (184.5)	ZMD-16	184.5	Quartz monzonite	North zone
11	ZMD12 (202.5)	ZMD-12	202.5	Biotite granite	South zone

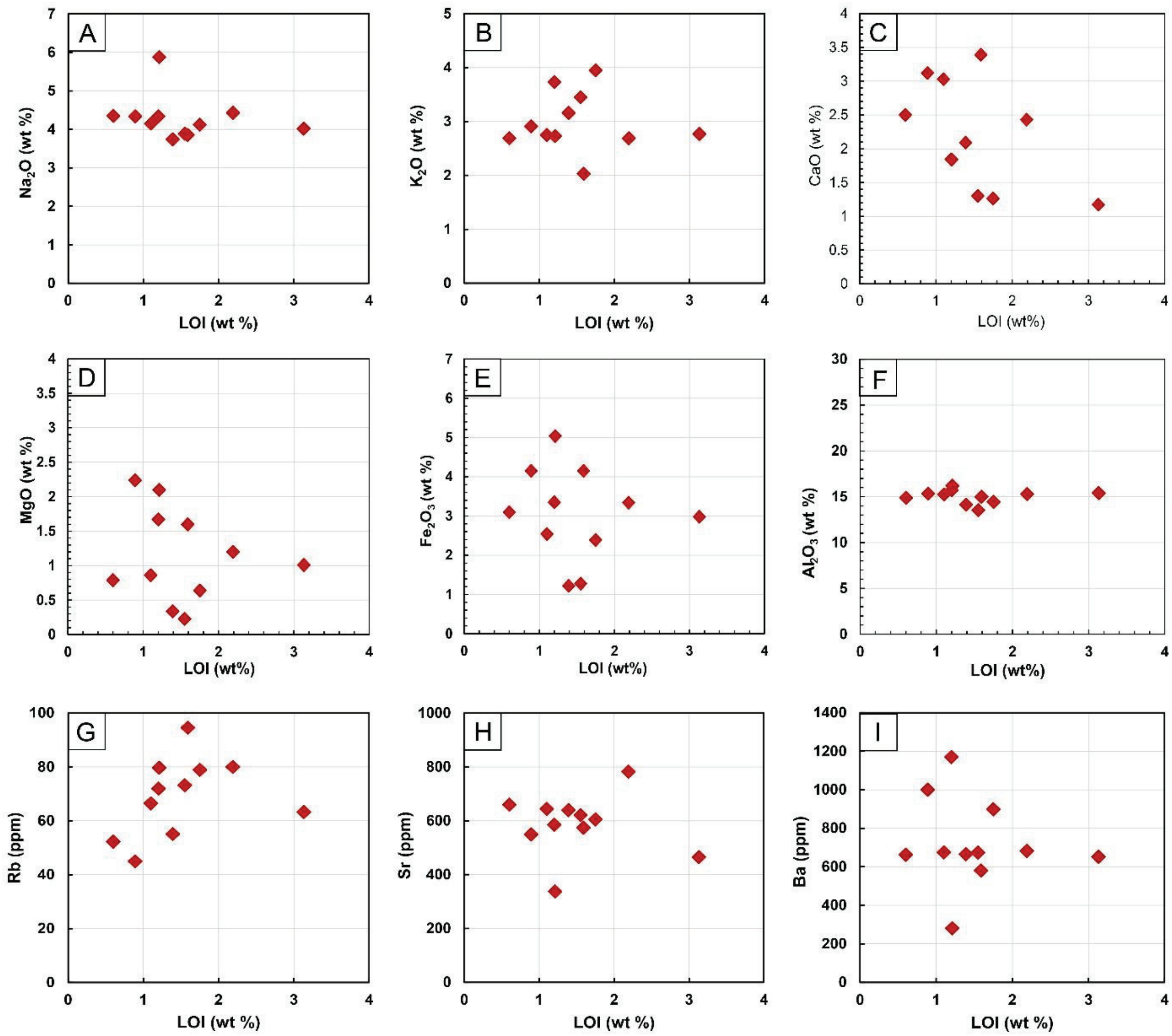

Fig. A2. Binary plots illustrating affects of hydrothermal alterations. A. Na_2O vs. LOI; B. K_2O vs. LOI; C. CaO vs. LOI; D. MgO vs. LOI; E. Fe_2O_3 vs. LOI; F. Al_2O_3 vs. LOI; G. Rb vs. LOI; H. Sr vs. LOI; I. Ba vs. LOI.

Appendix 3

Click here to access/download;Table (Editable version);Appendix-3.xlsx

Table A3-1. Blank measurements.

Sample run	Sample ID	Re (ng) Measured value		Common Os (ng)		Os187 (ng)	
			Uncertainty	Measured value	Uncertainty	Measured value	Uncertainty
060715-11	BK	0.00033	0.00031	0.00024	0.00005	0.00003	0.00002
060715-12	BK	0.00042	0.00055	0.00032	0.00005	0.00004	0.00005

Table A3-2. Measurement on the Standard GBW04435 (HLP).

Sample run	Sample ID	Sample weight (g)	Re (ng/g) Measured value	Uncertainty	Os187 (ng/g) Measured value	Uncertainty	Model age (Ma) Measured value	Uncertainty
060715-10	hlp	0.01	283809	2902	655	4	220	4
Accuracy			0.004		0.6		0.7	

Table A3-3. Certified values of the Standard (Stein et al., 1997)

		Re (μg/g) Measured value	Uncertainty	Os187 (ng/g) Measured value	Uncertainty	Model age (Ma) Measured value	Uncertainty
GBW04435 (HLP)		284	6	659	14	221	6

Appendix 4 Click here to access/download;Table (Editable version);Appendix-4.xlsx

Table A4. Accuracy and precision calculations of the standard and dublicate measurements of whole-rock geochemical data.

Standard ID	AMISO167		Certified value	Average value	Deviation from certified value (%)	External precision (2σ %)	OREAS146		Certified value	Average value	Deviation from certified value (%)	External precision (2σ %)
No	Lower	Upper					Lower	Upper				
SiO2 %	86.9	96	91.7	91.45	0	14						
TiO2	0.13	0.17	0.14	0.15	7	38						
Al2O3	2.29	2.55	2.37	2.42	2	15						
Fe2O3	3.27	3.63	3.46	3.45	0	15						
MnO	0.01	0.04	0.02	0.025	25	170						
MgO	0.22	0.26	0.22	0.24	9	24						
CaO	0.11	0.15	0.12	0.13	8	44						
Na2O	0.07	0.11	0.08	0.09	13	63						
K2O	0.47	0.54	0.47	0.505	7	20						
P2O5	0.01	0.05	0.03	0.03	0	189						
V ppm							140	182	163	161	1	37
Cr							180	240	190	210	11	40
Co							30	37.8	31.3	33.9	8	33
Ni							68	96	70	82	17	48
Cu							25	49	33	37	12	92
Zn							1230	1510	1410	1370	3	29
Rb							24.6	30.6	27.9	27.6	1	31
Sr							2790	3410	3310	3100	6	28
Y							814	996	954	905	5	28
Zr							180	280	230	230	0	61
Nb							349	427	408	388	5	28
Ta							3.8	4.8	4.4	4.3	2	33
Ba							10000	11450	10000	10725	7	19
Hf							4.6	6	5.1	5.3	4	37
Cs							0.47	0.59	0.54	0.53	2	32
Ga							26.2	32.2	23.4	29.2	25	29
La							2260	2760	2590	2510	3	28
Ce							4220	5160	4850	4690	3	28
Pr							493	603	579	548	5	28
Nd							1965	2400	2330	2182.5	6	28
Sm							397	485	463	441	5	28
Eu							114.5	139.5	124.5	127	2	28
Gd							323	395	335	359	7	28
Tb							42.5	51.9	45.6	47.2	4	28
Dy							202	246	216	224	4	28
Ho							33.1	40.5	36.8	36.8	0	28
Er							78.3	95.7	80.9	87	8	28
Tm							8.9	10.9	9.55	9.9	4	29
Yb							48.1	58.9	50	53.5	7	29
Lu							5.66	6.94	6.32	6.3	0	29
U							2.37	3.01	2.69	2.69	0	34
Th							813	993	966	903	7	28
Pb							607	753	711	680	4	30
Mo							52	68	62	60	3	38
W							22	30	30	26	13	44
Sn							40	52	47	46	2	37

Standard ID	SY-4		Certified value	Average value	Deviation from certified value (%)	External precision (2σ %)	ZMD-10				Average value	Exter precis (2σ %
No	Lower	Upper					Measured	Duplicate	Lower	Upper		
SiO2 %	47.4	52.4	51.8	50	4	14	73	73.3	71.3	75	73.2	4
TiO2	0.26	0.31	0.28	0	2	25	0.45	0.47	0.44	0.48	0.5	8
Al2O3	19.65	21.7	20.2	21	2	14	13.95	14	13.6	14.35	14.0	4
Fe2O3	5.89	6.53	6.05	6	3	15	1.41	1.42	1.37	1.46	1.4	5
MnO	0.09	0.13	0.11	0	0	51	0.01	0.01	0.01	0.02	0.0	80
MgO	0.47	0.54	0.49	1	3	20	0.12	0.12	0.11	0.13	0.1	14
CaO	7.64	8.46	7.75	8	4	14	0.71	0.72	0.69	0.74	0.7	6
Na2O	6.74	7.47	7.08	7	0	15	3.62	3.64	3.53	3.73	3.6	5
K2O	1.57	1.75	1.63	2	2	15	4.41	4.42	4.29	4.54	4.4	5
P2O5	0.11	0.15	0.13	0	0	44	0.11	0.1	0.09	0.12	0.1	25
V ppm	5	18	6	12	92	160	40	39	33	46	39.5	27
Cr	10	30	10	20	100	141	10	10	10	20	12.5	80
Co	1.7	3.9	2.4	3	17	111	1.8	1.8	1.2	2.4	1.8	54
Ni	5	19	7	12	71	165	5	5	5	10	6.3	80
Cu	5	17	8	11	38	154	224	222	207	239	223.0	12
Zn	78	108	100	93	7	46	30	28	23	35	29.0	34
Rb	49.3	60.7	58.4	55	6	29	110	109	104	115	109.5	8
Sr	1070	1310	1255	1190	5	29	852	851	809	894	851.5	8
Y	106.5	131.5	117.5	119	1	30	17.3	16.9	15.7	18.5	17.1	14
Zr	460	610	600	535	11	40	250	240	210	280	245.0	24
Nb	11.5	14.5	13.8	13	6	33	14.1	15	13.6	15.5	14.6	12
Ta	0.7	1.1	0.9	1	0	63	1	1	0.9	1.2	1.0	25
Ba	306	375	328	341	4	29	634	629	599	664	631.5	8
Hf	9.3	11.9	11.6	11	9	35	6.9	6.6	6.2	7.3	6.8	14
Cs	1.34	1.66	1.59	2	6	30	2.97	2.92	2.79	3.1	2.9	9
Ga	31.4	38.6	38.5	35	9	29	18.9	19	17.9	20	19.0	9
La	51.7	64.3	57.3	58	1	31	15.8	15.9	14.6	17.1	15.9	13
Ce	109.5	134.5	119	122	3	29	31.6	31.8	29.6	33.8	31.7	11
Pr	13.45	16.55	15.05	15	0	29	3.92	4	3.73	4.19	4.0	10
Nd	51.2	62.8	59.8	57	5	29	14.7	15.1	14.1	15.7	14.9	9
Sm	11.4	14	13.5	13	6	29	3.04	3.12	2.9	3.26	3.1	10
Eu	1.77	2.23	2	2	0	33	0.64	0.64	0.58	0.7	0.6	15
Gd	12.55	15.45	14.25	14	2	29	2.55	2.51	2.35	2.71	2.5	12
Tb	2.33	2.87	2.71	3	4	29	0.45	0.45	0.42	0.48	0.5	11
Dy	16.35	20.1	18.45	18	1	29	2.93	2.87	2.71	3.1	2.9	11
Ho	3.86	4.74	4.61	4	7	29	0.66	0.65	0.61	0.7	0.7	11
Er	12.75	15.65	14.45	14	2	29	1.97	1.94	1.83	2.08	2.0	11
Tm	2.06	2.54	2.31	2	0	30	0.32	0.31	0.29	0.34	0.3	13
Yb	13.3	16.3	14.95	15	1	29	2.21	2.18	2.06	2.33	2.2	10
Lu	1.88	2.32	2.19	2	4	30	0.37	0.35	0.33	0.39	0.4	14
U	0.66	0.94	0.78	1	3	49	4.74	4.84	4.5	5.08	4.8	10
Th	1.21	1.59	1.18	1	19	38	7.46	7.73	7.15	8.01	7.6	10
Pb	5	21	10	13	30	174	22	22	16	28	22.0	45
Mo	2	6	2	4	100	141	11	11	8	14	11.0	45
W	1	3	1	2	100	141	13	13	11	15	13.0	25
Sn	6	10	8	8	0	71	4	4	3	5	4.0	41

Declaration of interest

The authors of this research manuscript declare that there is no financial and/or personal interest, conflict of interest, or competing interest.

Credit author statement

Gankhuyag Altankhuyag: Conceptualization, Methodology, Investigation, Visualization, Writing – Original Draft, Data curation: Enkhjargal Boldbaatar; Writing – Review & Editing: Bolorchimeg N. Tunnell; Writing – Review & Editing: Jargalan Sereenen; Supervision, Review & Editing: Marek Locmelis; Writing – Review & Editing: Xiaofeng Li; Review & Editing: Akira Imai; Review & Editing.